

CYRUS



GW  AIAA
SHAPING THE FUTURE OF AEROSPACE

THE GEORGE WASHINGTON UNIVERSITY
WASHINGTON, DC

**Design/Build/Fly 2020-2021
Design Report**

Table of Contents	Page
<u>Acronyms and Nomenclature</u>	3
<u>1 Executive Summary</u>	4
<u>2 Management Summary</u>	5
<u>2.1 Schedule and Major Milestones</u>	6
<u>3 Conceptual Design</u>	7
<u>3.1 Mission Breakdown</u>	7
<u>3.2 Sub System Requirements</u>	9
<u>3.3 Scoring Sensitivity</u>	11
<u>3.4 Design Concepts and Decision Matrices</u>	12
<u>3.5 Final Aircraft Conceptual Sketch</u>	16
<u>4 Preliminary Design</u>	17
<u>4.1 Design Methodology</u>	17
<u>4.2 Design Sizing Trades</u>	17
<u>4.3 Aircraft Stability</u>	27
<u>4.4 Predicted Aircraft Performance</u>	28
<u>5 Detail Design</u>	29
<u>5.1 Dimensional Parameters</u>	29
<u>5.2 Sub System Architecture, Integration, and Dimensions</u>	29
<u>5.3 Structural Characteristics and Capabilities</u>	34
<u>5.4 Weight and Mass Balance</u>	38
<u>5.5 Flight and Mission Performance</u>	39
<u>5.6 Drawing Package</u>	40
<u>6 Manufacturing Plan</u>	46
<u>6.1 Materials and Manufacturing Processes Investigated</u>	46
<u>6.2 Major Component Manufacturing</u>	47
<u>6.3 Manufacturing Gantt Chart</u>	50
<u>7 Testing Plan</u>	51
<u>7.1 Ground Testing</u>	51
<u>7.2 Flight Testing</u>	52
<u>7.3 Schedule</u>	54
<u>8 Performance Results</u>	55
<u>8.1 Special Mission Component Testing Results</u>	55
<u>8.2 Flight Testing Results</u>	56
<u>9 Bibliography</u>	58

Acronyms and Nomenclature

α (AOA)	Angle Of Attack	GW	George Washington University
$\eta_{h/v}$	Horizontal/vertical tail dynamic pressure ratio	IMU	Inertial Measurement Unit
ρ_{∞}	Freestream air density	l_{sensor}	Length of sensor deployment cable
$\tau_{e/r}$	Angle of attack effectiveness of the elevator/rudder	$l_{h/v}$	Horizontal/Vertical Tail Moment Arm
ABS	Acrylonitrile butadiene styrene	L/D	Lift to Drag Ratio - Aerodynamic Efficiency
AIAA	American Institute of Aeronautics and Astronautics	LED	Light Emitting Diode
AVL	Athena Vortex Lattice	L.E. length	Leading Edge Length
b	Wing span	LIPo	Lithium Polymer
$b_{E/h/R/v}$	Elevator/horizontal tail/rudder/vertical tail span	M1	Mission 1 score
BEC	Battery Eliminator Circuit	M2	Mission 2 score
c	Chord length	M3	Mission 3 score
$C_{m_{\delta E/R}}$	Rate of change of coefficient of moment as a function of Elevator/Rudder deflection	MAC	Mean Aerodynamic Chord
$C_{L_{\delta h/v}}$	Horizontal/vertical tail curve slope	MSL	Mean Sea Level
c_d, C_D	Coefficient of Drag (2D), (3D)	n_x	Number of "x" quantity, or max quantity
c_l, C_L	Coefficient of Lift (2D), (3D)	RC	Remote Control
CAD	Computer-Aided Design	$S_{h/v}$	Area of the Horizontal/Vertical Stabilizer
CFD	Computational Fluid Dynamics	S	Wing Platform Area
CG	Center of Gravity	SD&R	Sensor Deployment and Retrieval
DBF	Design Build Fly	SMC	Special Mission Component
D	Drag Force	T_x	Time for "x" completion, or max time
EDF	Electric Duct Fan	V_{∞}	Freestream Air Velocity
ESC	Electronic Speed Controller	$V_{h/v}$	Horizontal/vertical tail volume coefficients
FEA	Finite Element Analysis	w_{sensor}	Weight of the sensor
GPS	Global Positioning System		

1. Executive Summary

This report presents the 2020/2021 George Washington University's submission to the Design/Build/Fly contest. Specifically, this report details the design, manufacturing, and testing of the "Cyrus" aircraft design and the "Party Time" sensor platform. The team was able to overcome numerous technical challenges and obstacles related to the pandemic to create a flight and mission capable aircraft, dubbed "Billy Ray Cyrus", for the *first* time in GW DBF's 5 year history.

The DBF competition objectives are to create an aircraft that could both transport multiple sensor devices in a cargo flight and deploy, tow, and retrieve a single sensor in a similar fashion to the AN/ALE-55 Fiber-Optic Towed Decoy. During towing, the sensor must remain aerodynamically stable and include a system of lights that is visible from the ground. The team created the aircraft platform and the sensor payload, along with the shipping containers and deployment and retrieval mechanism, to satisfy the competition objectives.

The Cyrus design is a single motor, high wing monoplane designed to transport 8 stored sensors and execute sensor towing from the empennage. The aircraft meets all mission requirements and is highly reliable, simple, modular, low cost, and completely manufacturable within one week. Party Time is a 7.32 in long cylinder, equipped with dihedral fins and six green LEDs rated at 160 lumens each.

GW DBF followed the standard aircraft design process steps of conceptual, preliminary, and detailed design, as prescribed in *Aircraft Design: A Conceptual Approach* [1]. During the conceptual design phase, the team decided to place a high priority on flight reliability, simplicity, manufacturability, and range. These priorities were used to select a semi-monocoque fuselage, high wing, conventional tail, and dihedral sensor design. The selected configurations and other major systems were sized and studied for performance during the preliminary design phase. Once the design was ready for full scale development, the detailed design phase defined the exact specifications of all components, interfaces, and systems were created and studied for structural and performance characteristics.

Party Time was 3D printed and assembled over the fall semester. Various tests were conducted to verify its aerodynamic stability and light visibility. Due to COVID-19 restrictions, the team was given a very limited window to build and test Cyrus prototypes. The team utilized a combination of materials and methods to construct the aircraft based on individual system needs. The first prototype, Billy Ray, was machined and assembled in one week. Billy Ray underwent around fifteen ground and flight tests throughout the month of January and was progressively modified based on each test result. Two successful empty flight tests were conducted, but transport and sensor flight tests will not be conducted until March.

Final size and performance capabilities of the finalized Cyrus design are shown below.

Table 1.1: Cyrus Aircraft Details and Performance Capabilities

Wingspan	Length	Empty Weight	Cruise speed	Engine Type	Power System
5 ft	4 ft 10 in	17 lbf	73.3 ft/s	E-Flite Power 160	x1 37V 10S 4500mAh LiPo

2. Management Summary

The team consists of 5 senior and 12 non-senior students who are organized into three groups: leadership, sub-teams, and senior design “contractors”, as shown in Figure 2.1. Each sub-team is composed of a sub-team lead and sub-team members who focus on a specific aspect of the project. The special mission component team oversees the development of the sensor, sensor deployment mechanism, and shipping containers.

GW DBF has two senior design “contractor” groups responsible for the design and integration of the wing and fuselage. The leadership team worked in conjunction with the senior design groups to create a “contract” for each group that details a statement of work, deliverables, requirements, and a delivery schedule for the group’s components. The schedule for all senior design milestones aligned with the greater GW DBF schedule. Senior design “contractor” groups interfaced with relevant GW DBF teams for design, manufacturing, integration, and testing purposes; and reported directly to GW DBF leadership.

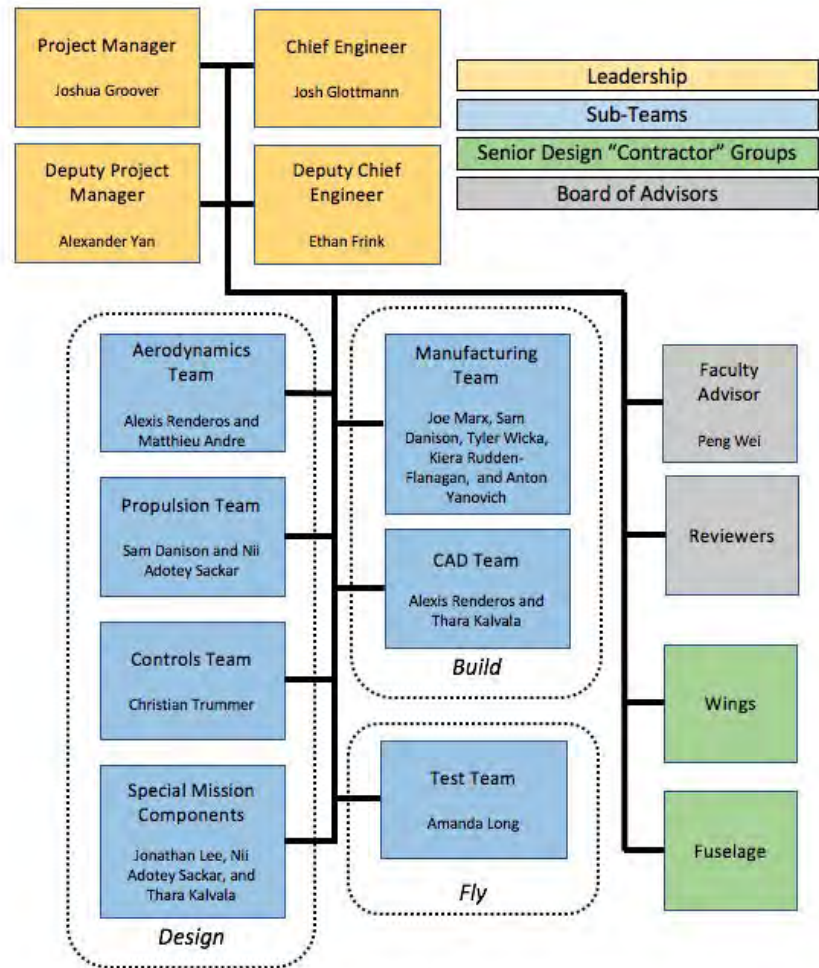


Figure 2.1: GW DBF Organization Chart

Additionally, the team had a Board of Advisors which was composed of GW DBF’s faculty advisor and an ad-hoc group of graduate students, faculty, and industry members. The faculty advisor regularly meets with the team, and acts as a mock customer and mentor. The Preliminary and Critical Design Reviews were presented to the Board of Advisors, who assessed the aircraft design and provided feedback to the team.

2.1 Schedule and Major Milestones

Figure 2.2 shows the major milestones, planned schedule, and actual progress for GW DBF. Some of the activities were delayed due to logistical issues, COVID-19 restrictions, and unexpected design challenges. The team is on track to build an aircraft that can accomplish all missions by early March.

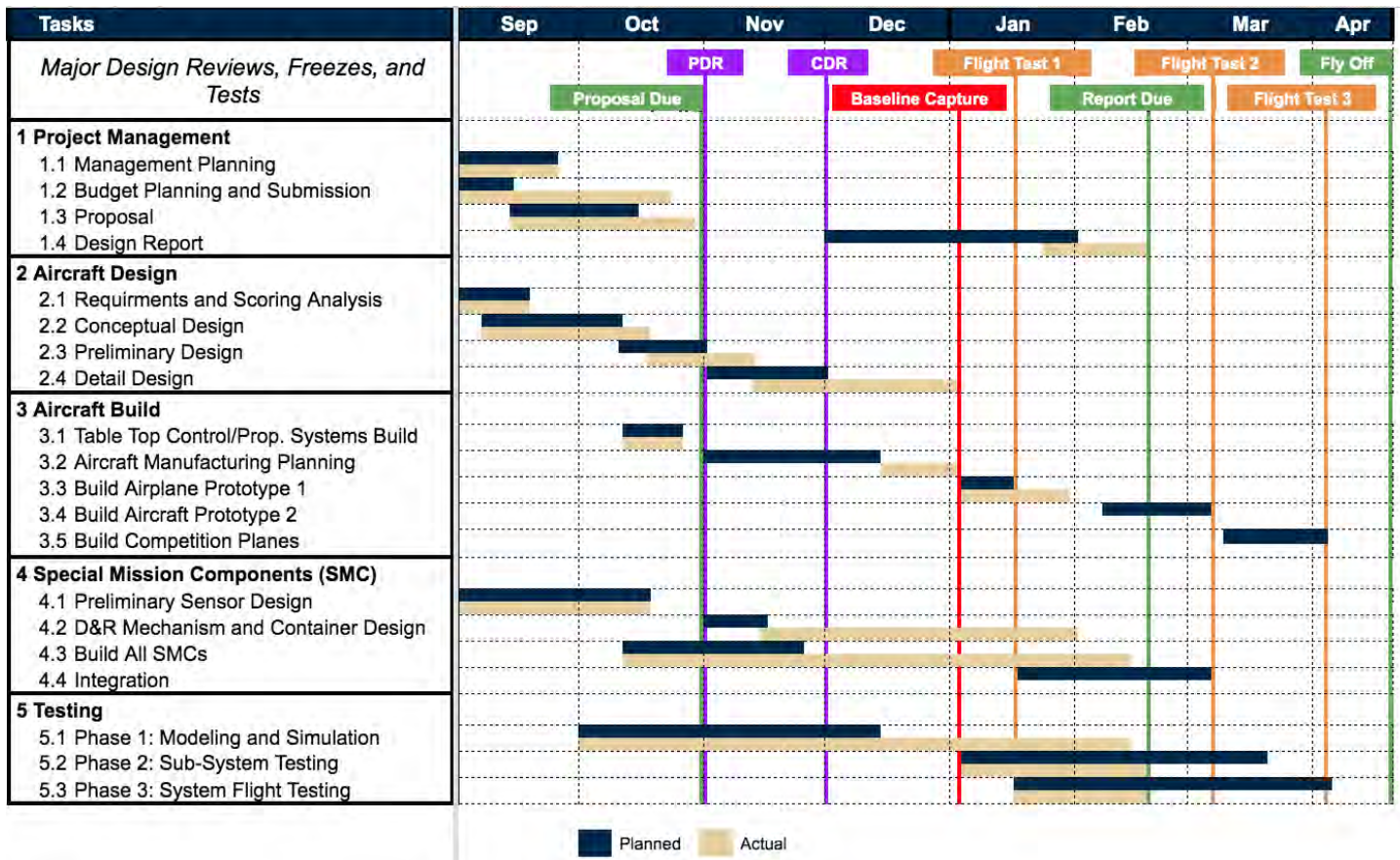


Figure 2.2: GW DBF Gantt Chart

3. Conceptual Design

The conceptual design phase was composed of two components: understanding the mission requirements and selecting the initial configuration of the aircraft. To achieve this, the team decomposed the missions, documented aircraft and sub system requirements, conducted a mission scoring sensitivity analysis, selected the major aircraft configurations, and created a final conceptual sketch of the aircraft.

3.1 Mission Breakdown

The problem and objective of the team is to design, build, and fly an aircraft capable of performing the following missions: a staging flight, delivery flight, and sensor flight. This section decomposes each of these and the Ground Mission. Prior to attempting any mission, the aircraft must pass the technical inspection outlined in the DBF Rules 2021 Final document. For all missions, the aircraft will fly in a pattern as shown in Figure 3.1. Each full pattern successfully flown by the aircraft is considered one lap.

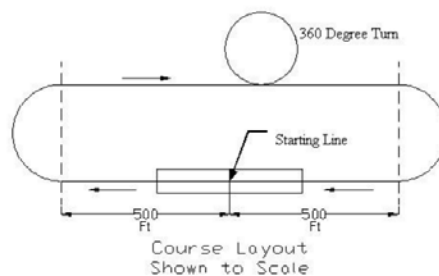


Figure 3.1: Flight Pattern

3.1.1 Mission 1: Staging Flight

The aircraft will be brought to the staging box in the flight configuration. Once the pilot advances the throttle for takeoff, the aircraft must take off within 100 ft and complete 3 laps within 5 minutes. After the 3 laps are completed, the aircraft must successfully land to receive a mission score. There is no cargo payload for Mission 1. The scoring breakdown for a successful mission is shown in Table 3.1.

Table 3.1: Mission 1 Scoring

Mission	Scoring Metric
Mission 1	$M1 = 1$

3.1.2 Mission 2: Delivery Flight

The goal of this mission is to transport the sensors inside the aircraft. The payloads for this mission are the sensor shipping containers, and the sensor deployment and retrieval mechanism. The aircraft can carry up to the amount of shipping containers declared in the technical inspection. The sensor deployment and retrieval mechanism will not be used in Mission 2, but the mechanism must be on board the aircraft. The loaded aircraft must take off within 100 ft of initiating ground roll and complete 3 laps within 5 minutes. The aircraft must successfully land to receive a score. The mission score is determined by the number of sensors the aircraft carries and the time the aircraft takes to complete 3 laps. The scoring breakdown is shown in Table 3.2.

Table 3.2: Mission 2 Scoring

Mission	Scoring Metric
Mission 2	$M2 = 1 + \frac{n_{GW \text{ containers}} / T_{GW}}{\max (n_{\text{containers}} / T)}$

3.1.3 Mission 3: Sensor Flight

The goal of this mission is to deploy, tow, and recover a sensor during flight. The payloads for this mission are the sensor, and sensor deployment and retrieval mechanism. The aircraft must take off within 100 ft with the sensor in the stowed configuration. Once airborne, the aircraft must deploy the sensor prior to completing the 360° turn on the upwind leg of the first lap. The aircraft will have 10 minutes from the time the throttle is advanced for takeoff to complete as many laps as possible. After the last 360° turn, the aircraft must fully retract and stow the sensor inside of the aircraft. Once the sensor is stowed, the aircraft must complete a successful landing to be scored. The mission score is determined by the number of laps completed, length of the sensor, and weight of the sensor. The scoring breakdown is shown in Table 3.3.

Table 3.3: Mission 3 Scoring

Mission	Scoring Metric
Mission 3	$M3 = 2 + \frac{n_{GW \text{ Laps}} * l_{GW \text{ Sensor}} * w_{GW \text{ Sensor}}}{\max (n_{\text{Laps}} * l_{\text{Sensor}} * w_{\text{Sensor}})}$

3.1.4 Ground Mission

The goal of the ground mission is to demonstrate the ability of the shipping container to protect the sensor and the aircraft's performance capabilities in Missions 2 and 3. First, the assembly crew member will load the sensor into the shipping container, drop the container on 6 sides from a height of 10 in, remove the sensor from the shipping container, demonstrate the sensor meets all functional requirements, and replace the sensor in the shipping container. Next, the team will be timed to reconfigure the aircraft into the Mission 2 and 3 setups. A ground mission official will say "Go" then an assembly team member will run to the aircraft, configure the aircraft for Mission 2, and run back to the starting line. The pilot will demonstrate that the flight controls are active. After the demonstration, the ground mission official will again say "Go", the assembly crew member will configure the aircraft for Mission 3, and run back to the starting line. The pilot will demonstrate that the flight controls are active and that the deployment and retrieval mechanism is functional. The mission score is a function of the time it takes to configure the aircraft for Missions 2 and 3. The full scoring breakdown is shown in Table 3.4

Table 3.4: Ground Mission Scoring

Mission	Scoring Metric
Ground Mission	$GM = \frac{T_{Min}}{T_{GW}}$

3.2 Sub System Requirements

After decomposing the missions, the team conducted a thorough analysis of the competition and general engineering requirements for the aircraft. Competition requirements were determined and weighted based on the team's interpretation of the rules document. General engineering requirements were discussed and decided upon by the team. A House of Quality study was conducted to analyze and trace the relationship and importance of competition requirements within the context of the general engineering requirements. The House of Quality is shown in Figure 3.2. The study determined that the team should primarily focus on addressing range, manufacturability, simplicity, and reliability requirements. Size, weight, reliability, maneuverability, affordability, and drag were considered, but only as a secondary priority for the design.

A detailed list of requirements was then compiled. Explicit requirements were gathered from the rules document and the team derived additional requirements based on the rules document, House of Quality, basic RC principles, and internal team objectives. The final set of requirements was utilized during all design phases to inform the team of minimum expected aircraft performance and create testing plans for system verification. The following sections describe the requirements for system sizes, aircraft performance, mission performance, and the propulsion and power systems. Explicit and derived requirements are marked with an (E) and (D) respectively.

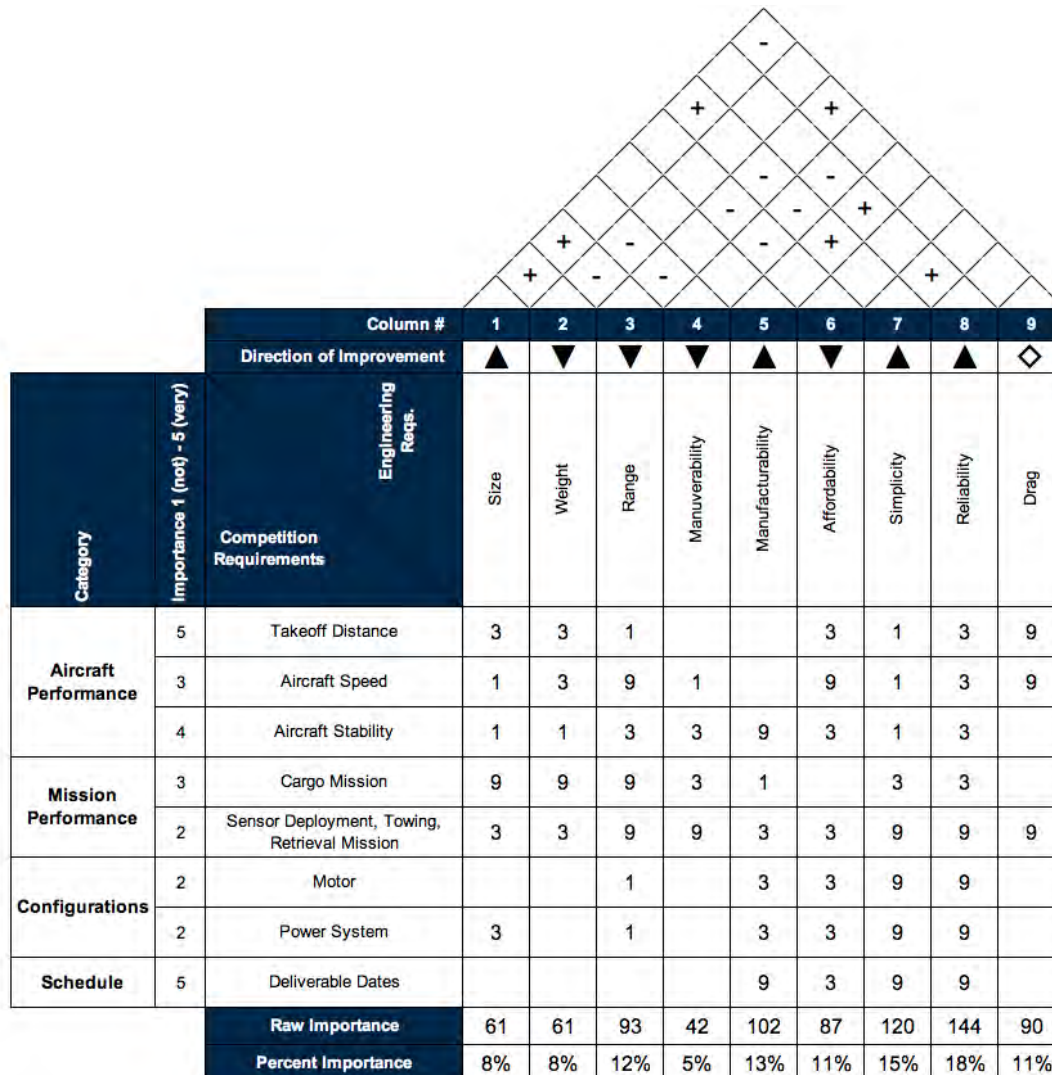


Figure 3.2: Requirements House of Quality

3.2.1 General

- (D) The aircraft sub-components shall be manufacturable within two weeks.
- (D) All system design shall favor simplicity if increasing complexity results in marginal benefit.
- (D) All system designs and materials shall favor minimizing weight to the extent possible.
- (D) The cost of building two prototype aircraft shall be less than \$2,280.
- (D) The cost of building three competition aircraft shall be less than \$3,260.

3.2.2 Aircraft, Sensor, Tow Cable, and Shipping Container Sizes

- (E) The aircraft wing span shall be no more than 5 ft.
- (E) The aircraft shall weigh no more than 55 lb in any configuration.
- (D) The aircraft center of gravity shall be between 25-30% MAC in all configurations.
- (E) The sensor shall have a minimum diameter of 1.00 in.
- (E) The sensor shall have a minimum length to diameter ratio of 4.
- (E) The tow cable shall be at least ten times the length of the sensor.
- (E) The shipping container shall fully enclose the sensor.
- (E) Simulator shipping containers shall:
 - have dimensions within $\frac{1}{8}$ " in. of the packed shipping container.
 - weigh greater than or equal to the packed shipping container.

3.2.3 Aircraft Performance

- (D) The aircraft shall have a minimum cruising velocity of 35 ft/s without the sensor deployed.
- (D) The aircraft shall have a minimum climb and descent rate of 1.84 ft/s.
- (D) The aircraft shall have a range of at least 35,000 ft while the sensor deployed.
- (D) The aircraft shall have a flight reliability above 85% during normal operating conditions.
- (E) The aircraft shall take off in all configurations within 100 ft of beginning a takeoff run.
- (D) The aircraft shall be capable of operations on well-maintained paved, grass, and dirt runways.
- (D) The aircraft shall maintain static and dynamic stability during flight.
- (E) The wing structure shall support the weight of the fully loaded aircraft.
- (E) During a radio signal loss, the aircraft receiver shall default the control system to the following configuration: throttle closed, full up elevator, full right rudder, full right aileron, and full flaps down.

3.2.4 Mission Performance

- (E) For the delivery mission:
 - The sensor shall be transported inside a shipping container.
 - A shipping container with the sensor shall be secured and transported inside the aircraft.
 - Simulator shipping containers shall be secured and transported inside the aircraft.
- (E) For the sensor mission a SD&R mechanism shall deploy, tow, and retrieve the sensor.
- (E) The SD&R mechanism shall be fully enclosed within the aircraft.
- (E) The sensor shall be fully enclosed within the aircraft before deployment and after retrieval.
- (E) All commands sent to the sensor shall occur through a physical electrical connection between the sensor and sensor deployment and retrieval mechanism (e.g. aircraft).

- (E) Sensor deployment, towing, and retrieval shall not affect the aerodynamic stability of the aircraft.
- (E) The sensor shall be aerodynamically stable during deployment, operation, and recovery.
- (E) The sensor shall have a minimum of 3 external lights.
- (E) The sensor lights shall:
 - operate one at a time in a pattern.
 - be visible by the Flight Director.
 - be turned on and off remotely via the flight or payload transmitter.
 - contain its own battery power supply which is compliant to all previously noted power requirements.
- (E) The shipping container shall protect the sensor from drop shock events.

3.2.5 Propulsion and Power Systems

- (E) The motor shall be an off the shelf propeller motor or EDF.
- (E) The motor shall use commercially available propeller blades.
- (E) The motor shall have an external safety switch.
- (E) The power system batteries shall be LiPo or NiCad, but not both.
- (E) The power system batteries shall not be in series.
- (E) If multiple batteries are utilized for the power system, there shall be a 0.25 in air gap between each installed battery onboard the aircraft.
- (E) If multiple batteries are utilized to power a single system, all batteries shall be identical brands and ratings.
- (E) The power system batteries shall be less than or equal to 100 Wh.
- (E) Each LiPo battery in the power system shall have a fuse.
- (E) The power system shall have a fuse or arming plug that is behind the propeller for tractor aircraft.

3.3 Scoring Sensitivity

The requirements and mission information were used to conduct a scoring sensitivity analysis. Baseline estimates for GW and top performance for each flight mission are shown in Figure 3.3. One way sensitivity analysis was used to measure GW's total score change when the design parameters were changed. Designing the aircraft to maximize one of the parameters could result in a marginal total score increase, but could push the physical limits of the aircraft and reduce flight reliability. A failure on Missions 2 or 3 would result in loss of the “free points” awarded for successful mission completion that are not dependent on performance. A design that executes all the previously defined requirements with high reliability is the best option to score well in the fly-off.

The results underscore the importance of designing for reliability. Aircraft testing requires multiple flight tests within a limited timeframe. Having an aircraft with high flight reliability will allow GW DBF to conduct more flight tests and reduce the likelihood an aircraft will be significantly damaged due to a failure. More testing translates to more design improvements, which will increase the aircraft's probability of success during the fly-off.

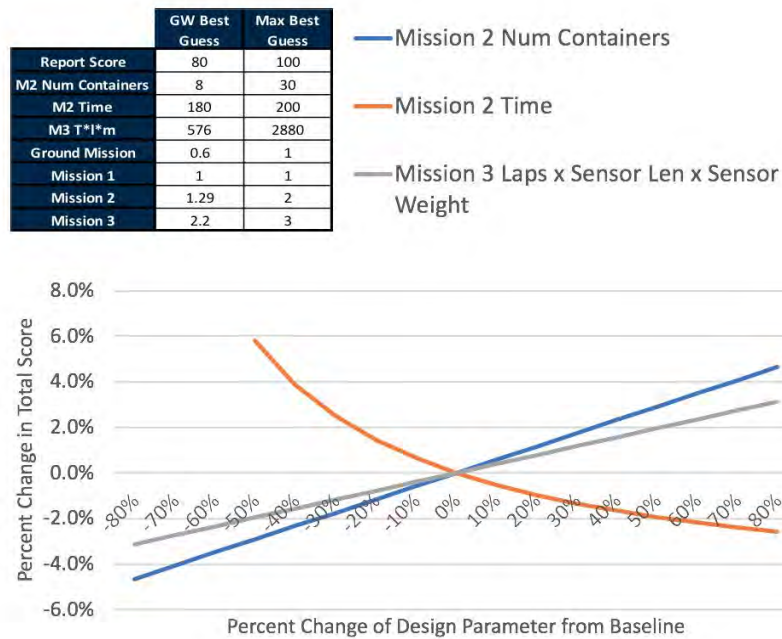


Figure 3.3: One Way Scoring Sensitivity Analysis

3.4 Design Concepts and Decision Matrices

The team utilized the requirements and scoring sensitivity analysis to identify options for major system configurations. For each major system, requirements and other relevant considerations were utilized to create selection figures of merit. Potential configurations were compared and selected using a weighted decision matrix. A final conceptual design of the aircraft is shown in Figure 3.4.

3.4.1 Fuselage

Four fuselage structures were considered: truss, geodetic, square monocoque, and square semi-monocoque. A truss structure is an arrangement of trusses, which distributes structural loads evenly throughout the fuselage and offers a variety of interfacing points while being relatively strong. A geodetic structure is a shell shaped fuselage with a pattern of members laid across the inside of the shell, which provide strong support against torsional loading. Both of these structures have high weights, are challenging to manufacture within a short timeline, and increase system complexity with marginal structural benefit. A square monocoque structure utilizes a thin shell to handle loading. The skin of the shell handles a large portion of shear forces, while the square shape can easily interface with many other components attached to the fuselage. However, there are very few high strength low weight skins available at the RC scale. A square semi-monocoque fuselage is a lighter weight structure that allows for easy interfacing and has good axial and torsional support properties. The weighted decision matrix used to select the fuselage structure is shown in Table 3.5 and a square, semi-monocoque fuselage structure was selected. An additional benefit of this selection was that a semi-monocoque system was easy to model with structural idealizations, which streamlined design stress analysis.

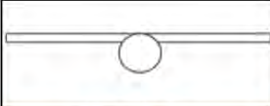
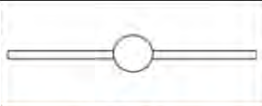
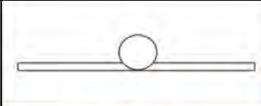
Table 3.5: Decision Matrix for Fuselage Structure

Criteria	Weight	Truss	Geodetic	Square Monocoque	Square Semi-Monocoque
Interfacing	30%	3	1	1	3
Strength	30%	3	3	3	5
Manufacturability	20%	1	1	5	3
Weight	20%	1	1	3	3
Weighted Score		2.2	1.6	2.8	3.6

3.4.2 Wing Placement

The wing's location on the aircraft affects its handling, manufacturability, and cargo access. Three wing placement options were considered: high wing, mid wing, and low wing. A high wing configuration provides a very stable flying platform because the center of lift is above the center of gravity, reducing ground effect during takeoff and landing. A mid wing configuration provides a more maneuverable platform; however, the mid wing's attachment point takes up space in the fuselage and limits cargo capacity. A low wing configuration provides the least stable and most maneuverable platform, but has the lowest reliability due to the higher risk of damage from a wing to ground strike during takeoff or landing. Both the mid and low wings would need to be made in two pieces, increasing design and manufacturing complexity, but they both allow for easy cargo loading from the top of the fuselage. Cargo accessibility was more challenging for the high wing, as cargo would need to be loaded underneath the wing from the sides of the fuselage. The weighted decision matrix for wing placement is shown in Table 3.6 and a high wing was selected.

Table 3.6: Decision Matrix for Wing Placement



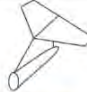
				
Figure of Merit	Weight	High Wing	Mid Wing	Low Wing
Flight Stability	30%	5	3	1
Cargo Access	30%	3	1	5
Manufacturability	20%	5	1	3
Reliability	20%	5	3	1
Weighted Score		4.4	2	2.6

3.4.3 Empennage

Three potential empennage configurations were considered: conventional tail, T-tail, and swept tail. The conventional tail is the most simple configuration and performs necessary trimming, controlling, and stabilizing functions. In a conventional configuration, the horizontal tail creates longitudinal trim and stability, and the vertical tail creates the directional trim and stability. The simplicity, manufacturability, and overall tail performance of the conventional design makes it a widely adopted choice. The swept tail configuration consists of a swept-back stabilizer, which, like a swept wing, is meant to decrease potential wave drag [2]. More applicable to the assigned missions, at low speeds, the swept tail configuration

improves the sideslip characteristics of the tail surfaces [3], which improves aircraft stability. The T-tail configuration consists of a horizontal tail section on top of a vertical tail section forming a “T” shape. In this configuration, the horizontal stabilizer and elevator are moved out of the wing wake and downwash, reducing aerodynamic interference during pitching maneuvers. However, the T-tail can result in a deep stall [4] and would require a more structurally rigid vertical component, increasing total empennage weight. The weighted decision matrix for the empennage configuration is shown in Table 3.7 and a conventional tail was selected.

Table 3.7: Decision Matrix for Empennage Configuration

				
Figure of Merit	Weight	Conventional	Swept	T-tail
Manufacturability	30%	5	3	1
Simplicity	30%	3	1	1
Weight	20%	5	3	3
Stability	20%	3	5	1
Weighted Score		4	2.8	1.4

3.4.4 Landing Gear Configuration

Three landing gear configurations were considered: conventional, tricycle, and four-wheeled. Conventional landing gear provides a higher ground clearance at the front of the plane, higher angle of attack on takeoff, and is more forgiving on grass surfaces. However, conventional landing gear requires a structurally reinforced hardpoint for the tail wheel, which increases tail weight and structural complexity. Tricycle landing gear interface directly into the fuselage, which reduces structural complexity. In addition, tricycle landing gear are easier to land on because the gear orientation is the same as the flare orientation. A four-wheel landing gear in a conventional configuration, where the rear bracket is slightly shorter than front, provides the structural simplicity of tricycle landing gear while increasing operating performance on terrains like grass and dirt. However, this configuration makes turning the aircraft on the ground more difficult. Larger wheels will be utilized for all configurations, as they perform better on grass and dirt terrain than smaller wheels. The weighted decision criteria are shown for each configuration in Table 3.8 and the four-wheel conventional landing gear was selected.



Table 3.8: Design Decision Matrix for Landing Gear Configuration

				
Criteria	Weight	Conventional	Tricycle	4-Wheel Conventional
Takeoff Performance	35%	4	5	5
Terrain Capability	25%	4	1	5
Manufacturability	25%	3	4	4
Stability	15%	3	4	5
Weighted Score		3.6	3.6	4.75

3.4.5 Sensor Deployment Location

Two sensor deployment locations were considered: under the center of the fuselage and from the empennage. Towing the sensor from under the fuselage provides the most stability as it is closer to the CG. However, a deployment mechanism located in this area will reduce cargo storage capacity and highly interfere with other components, which significantly increases the implementation complexity. If the sensor is heavy, deploying from the empennage could have adverse effects on the stability of the aircraft. The empennage, however, has much greater storage capacity and this deployment location would minimize interference with the tail, landing gear, and other components. The weighted decision criteria for each location is shown in Table 3.9 and the empennage sensor deployment location was selected.

Table 3.9: Design Decision Matrix for the Sensor Deployment Location





			
Criteria	Weight	Fuselage	Empennage
Stability	30%	5	3
Storage Capacity	30%	2	5
Simplicity	20%	2	5
Interference (low)	20%	1	3
Weighted Score		2.7	4

3.4.6 Sensor Fin Design

A cylinder with a nose cone was selected as the base sensor body shape. Four sensor fin designs were considered: no fins, a large rudder, “X” pattern fins, and a dihedral. Having an aerodynamically stable sensor was the most significant selection criteria because it was a direct requirement of the competition. In addition, sensor aerodynamic stability enables smooth deployment and retrieval, predictable flight characteristics, and more consistent external light visibility. All sensor fin designs were 3D printed and tested to determine their aerodynamic behavior (See sections 7.1.2.1 and 8.1.2).

The plain cylinder design had low drag and high storage density for the cargo mission, but the absence of fins resulted in lower aerodynamic stability. The large rudder design maintains an upright flight orientation, but behaved chaotically and had a low storage density. The X-Fin’s symmetric shape had significantly more stability than the previous options with moderate storage density and drag. The dihedral fin design best maintained an upright attitude and stability during testing, likely due to the dihedral effect, and had a higher cargo storage density than the rudder or x-fin designs. The weighted decision matrix for sensor fin design is shown in Table 3.10 and the dihedral fin design was selected.




Table 3.10: Design Decision Matrix for Sensor Shape

					
Criteria	Weight	Cylinder	Large Rudder	X fins	Dihedral
Stability	65%	1	3	4	5
Storage Density	25%	5	2	3	4
Drag (low)	10%	5	4	3	1
Weighted Score		2.4	2.85	3.65	4.35

3.4.7 Sensor Shipping Container

Three designs were considered for the sensor shipping container: a rectangular prism, triangular prism, and football shaped container. Each design was scored based on its simplicity, ability to protect the sensor from drop shock events, and cargo storage capacity within the fuselage. The rectangular box was the simplest design with moderate storage capacity, however the triangular prism had the most storage capacity. Additionally, the triangular shipping container maintained simplicity and protected the sensor slightly more than the rectangle. The football shaped design would protect the sensor the best, however, it was the least efficient space wise and most difficult to secure to the plane. The scores of each shipping container design are shown in Table 3.11 and a triangular prism was selected.

Table 3.11: Design Decision Matrix for Sensor Shipping Container

				
Criteria	Weight	Rectangular	Triangular	Football
Storage Capacity	40%	3	5	2
Simplicity	30%	5	5	1
Sensor Protection	30%	2	3	5
Weighted Score		3.3	4.4	2.6

3.5 Final Aircraft Conceptual Sketch

The decision matrices and requirements were utilized to create a finalized conceptual design sketch shown in Figure 3.4.

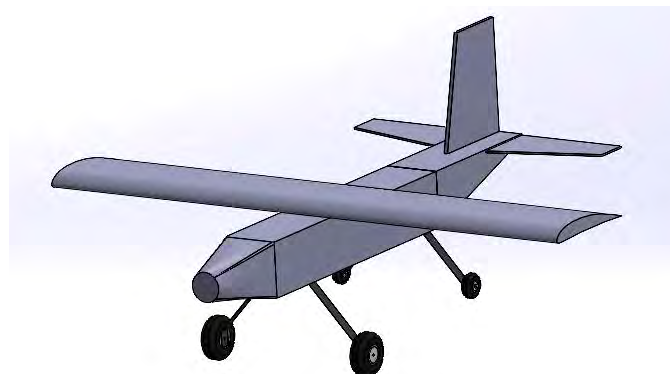


Figure 3.4: Final Conceptual Aircraft Sketch

4. Preliminary Design

The preliminary design phase was an iterative process where major systems were sized, evaluated using a variety of analysis techniques, and resized to improve performance and structural characteristics. Applying these analysis techniques iteratively drove sizing decisions and analysis techniques for the fuselage materials, airfoil selection, chord length, control surfaces, servo torque, propulsion system, and sensor. Detailed information regarding the lift, drag, static, dynamic stability, and predicted aircraft performance was determined to assess the design's readiness for full-scale development.

4.1 Design Methodology

After the conceptual design of the aircraft was completed, the team began analyzing and sizing the individual parts. Iterative use of several analysis options such as CFD in SolidWorks, stability analysis in AVL, and other computational tools allowed for efficient design improvements. Due to scheduling constraints and COVID-19 restrictions, the team used SolidWorks CAD and CFD packages to obtain a representation of the aerodynamic effects instead of prototyping or wind tunnel testing. The analyses in AVL produced stability derivatives for a chosen design to quantitatively demonstrate stability requirements were met. Thrust calculators allowed the team to appropriately size the relative motor power configuration, providing an alternative to purchasing, testing, and comparing various motor models. Parameters such as weight, takeoff distance, cruising speed, wing area, and other aircraft performance characteristics were determined to address mission requirements specified by the competition.

4.2 Design Sizing Trades

4.2.1 Fuselage Stringer Material

Stringers, in a semi-monocoque design, create the main shape of the fuselage and distribute the structural and aerodynamic loads experienced during flight. The stringers play a critical role in maintaining structural stability and interfacing the fuselage with other aircraft systems. In the square fuselage configuration, extruded angles were used as stringers instead of a typical rod because they offer similar performance characteristics, more fuselage space for cargo, and integrate better with the nose cone, wing, and empennage.

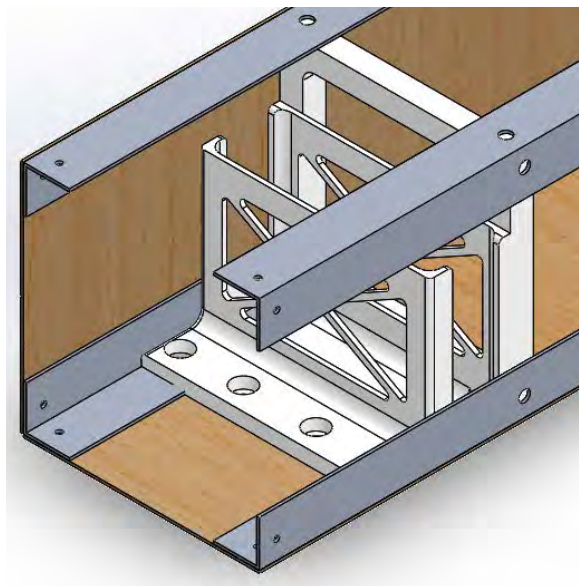


Figure 4.1: Sample Aluminum L-Bracket Stringer Fuselage

The stringer material needed to be strong and easily manufacturable, while providing enough flexibility to withstand torsional loads. Two materials were considered: carbon fiber and aluminum. Carbon fiber's impressive strength-to-weight ratio made it a promising choice, while aluminum is an inexpensive, relatively light, easily machined metal with high strength to weight ratio.

Table 4.1: Strength, Density, and Cost of Carbon Fiber and Aluminum

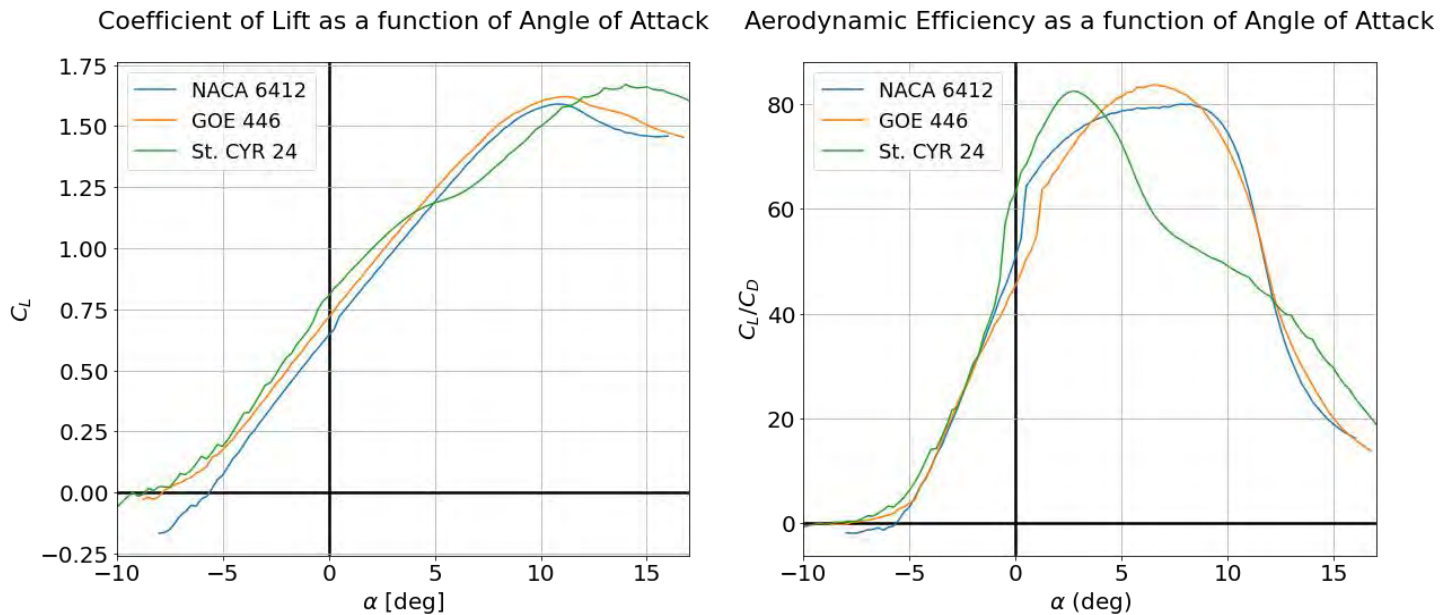
	Solid CF Carbon Fiber	Aluminum 6061
Tensile Strength (MPa)	919	308
Density (g/cm³)	1.41	2.7
Specific Strength (kN-m/kg)	652	114
Angle Bracket Cost (\$/ft)	31.67	1.4

The tensile and specific strengths, density, and cost per angle bracket for carbon fiber and aluminum were compared, as shown in Figure 4.1. Carbon fiber had a higher specific strength and lower density than aluminum, making it ideal in terms of its physical properties. However, the cost of a carbon fiber angle bracket was prohibitively expensive. Aluminum was well within the strength requirements for the stringers and a much more cost effective option than carbon fiber. As such, aluminum was selected as the stringer material.

4.2.2 Airfoil Selection

Several criteria were considered for airfoil selection. First, the airfoil needed to produce sufficient lift during takeoff and cruise configurations to support the anticipated weight of the aircraft during delivery flight. Second, the airfoil needed to have a high lift to drag ratio during cruise flight. This was especially important for the sensor mission where range and battery endurance were the keys to successfully completing the mission. Third, manufacturing a complex airfoil shape in-house at GW would be difficult. Airfoil shapes were kept simplistic to increase the manufacturability and simplicity of the design. Finally, the airfoil was required to have a minimum thickness of at least one in to accommodate the wing spar. The top three airfoil options considered were the NACA 6412, the St. CYR 24 (Bartel 35-IIIC), and the Glottingen (GOE) 446 airfoils found from the Airfoil Tools online database [5].

Graphs for coefficient of lift vs. angle of attack and aerodynamic efficiency, or coefficient of lift divided by coefficient of drag, were generated using CFD and are presented in the following Figures 4.2A and 4.2B, respectively. These graphs were generated with a Reynolds number of 200,000, which is the closest value to the anticipated number of 360,000 available in the analysis tool utilized. This anticipated Renolds number was approximated using a velocity of 55 ft/s, and a chord length of 12.



Figures 4.2A and 4.2B: Lift and Drag Characteristics of Analyzed Airfoils at a Reynold's Number of 200,000

A level flight, or 0° angle of attack, was assumed for the cruising angle of attack. The coefficient of lift near this AOA ranges from 0.65 to 0.85 for all three airfoils. While the empty aircraft was not expected to weigh more than 13 lbf, the airfoil was selected for a “worst case” gross takeoff weight of 20 lbf. The worst case scenario serves as a safety buffer and designing for it would increase flight reliability for the transport mission. The minimum coefficient of lift necessary for a cruise velocity of 80 ft/s and weight of 20 lbf was 0.57. This suggests that the highly loaded configuration for the transport mission could be supported by all airfoils during cruise. An airfoil with a high cruising efficiency would reduce the power consumption from the motor and result in a higher range and endurance for the sensor mission. At the cruising AOA, the St. CYR 24 had a higher lift to drag ratio compared to the GOE 446 and NACA 6412. As such, the St. CYR 24 had a longer range and higher endurance than the other airfoil options.

Another important consideration was the stall regions of each airfoil. The takeoff AOA was assumed to be 10° due to the landing gear configuration on the ground. While the NACA 6412 and GOE 446 stall around 11° and 12° respectively, the St. CYR 24 stalls at a higher 13.75° . The additional operating range gave the pilot more room for error during takeoff and landing and will increase the aircraft's flight reliability.

Between 5° and 10° AOA, the NACA 6412 and GOE 446 were significantly more efficient than the St. CYR 24; however, this AOA range will only be experienced for short durations when durinclimbing to cruise altitude or descending to land. Cruising flight efficiency, endurance, range, and reliability were higher priority for the airfoil selection than the climb and descent efficiency for the airfoil. As such, the team selected the St. CYR 24 airfoil. Additionally, a wingspan of 5 ft was selected to account for the high wing loading of the aircraft while complying with the competition requirements.

4.2.3 Chord Length Sizing

The goal of chord length sizing was to find a length that generated enough lift for the expected aircraft weight while minimizing total wing weight. Parametric SolidWorks CFD analyses, with default meshing, were conducted on 6, 8, 10, 12, and 16 in chord lengths for the St. CYR 24. Input velocities and AOAs were used to determine the lift generated by the wing. A sample result for the 12 in chord is shown in Figure 4.3.

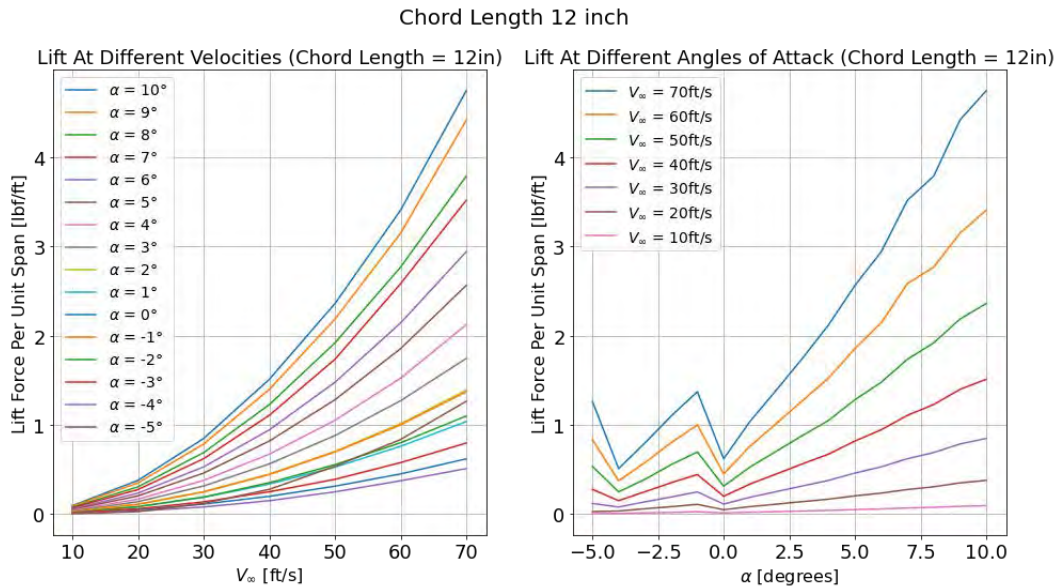


Figure 4.3: Lift Generated by a 12 in Span, 12 in Chord Length

As shown in the figures, chord length and lift generated are directly related. To take off and cruise for the worst case scenario, the wing must generate at least 20 lbf of lift. Figure 4.4 shows a comparison of the chord lengths and lift produced at various velocities for the takeoff AOA of 10° . At the expected takeoff velocity of 52 ft/s, the 16 and 12 in chord lengths produced equal to or greater than the lift requirement of 4 lbf/ft, while the 6, 8, and 10 in chord lengths did not.

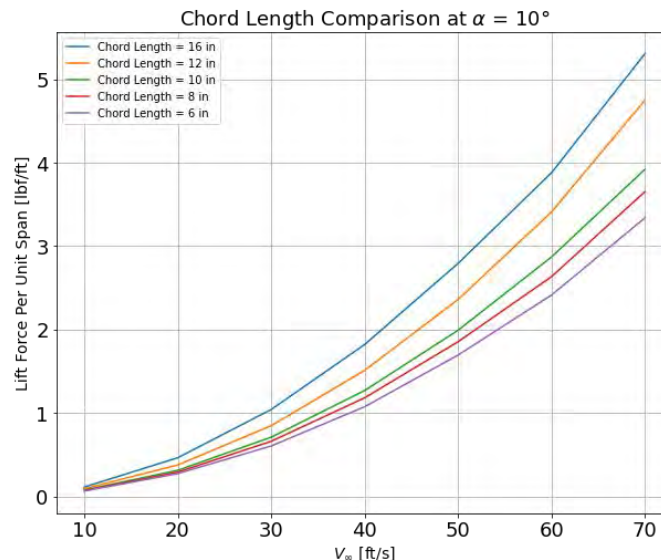


Figure 4.4: Lift Generated by All Chord Length Studies at 10° AOA

As the chord length increases, the total wing weight increases as well. Weight was used to determine which chord length to select, as the requirements state that the design shall favor minimizing weight if function is not affected. Volume was used as a proxy for weight and the total volume for the 12 and 16 in wings is shown in Table 4.2. The 12 in chord had significantly less volume than the 16 in chord, which would reduce the thrust needed to fly the aircraft. Minimizing needed thrust is critical for finishing the sensor mission, as a lower thrust translates to longer battery life and a longer flight.

Table 4.2: Volume Properties of Different Chord Lengths, Given for 1 in Spans

Chord Length	Volume (in ³)	Volume Ratio V_i / V_{12in}
12	12.6	1
16	22.36	1.775

The 12 in chord generated enough lift for the worst case scenario while minimizing wing weight. As such, a 12 in chord was selected for the wing.

4.2.4 Control Surfaces: Sizing and Location

This section presents the analysis used to determine the sizing and location of the ailerons, elevator, and rudder. Major considerations for these selections included aircraft stability, weight, and control authority.

For appropriate pitching control, the design considers the rate of change of the moment coefficient with respect to elevator deflection, which is given by equation 4.2. This is primarily a function of the horizontal tail lift curve slope, the horizontal tail volume coefficient, and the horizontal tail dynamic pressure ratio [4]. Additionally, the elevator angle of attack effectiveness is primarily a function of elevator-to-tail chord ratio [4]. Similarly for yawing control, the equation for coefficient of moment with respect to rudder is given by equation 4.3. An angle of deflection of $\pm 16.5^\circ$ for the rudder and an angle of deflection of $\pm 8.5^\circ$ for the elevator was selected to produce adequate coefficients of moment.

$$C_{m_{\delta E}} = -C_{L_{\alpha_h}} \eta_h V_h \frac{b_E}{b_h} \tau_e \quad (4.1)$$

$$C_{m_{\delta R}} = -C_{L_{\alpha_v}} \eta_v V_v \frac{b_R}{b_v} \tau_r \quad (4.2)$$

To determine the aileron location and size, the rolling moment from various aileron sizes and locations was analyzed using SolidWorks CFD with default meshing. Each colored line represents a different lateral location of the aileron along the wing. The further away the aileron was from the wing tip, the lower the rolling moment. At the wing tips, all of the aileron sizing designs produced adequate rolling moment, so the team considered other aspects of the design. The team decided to keep the ailerons beyond the 50% wingspan points to avoid propeller wash over the ailerons. This ensured stability during rolling, and by extension, increased flight reliability. Additionally, the ailerons were slightly reflexed to move the center of pressure forward near the wing tips. This reduces the likelihood of a tip stall, increased flight reliability, and stability.

Aileron Sizing Comparisons

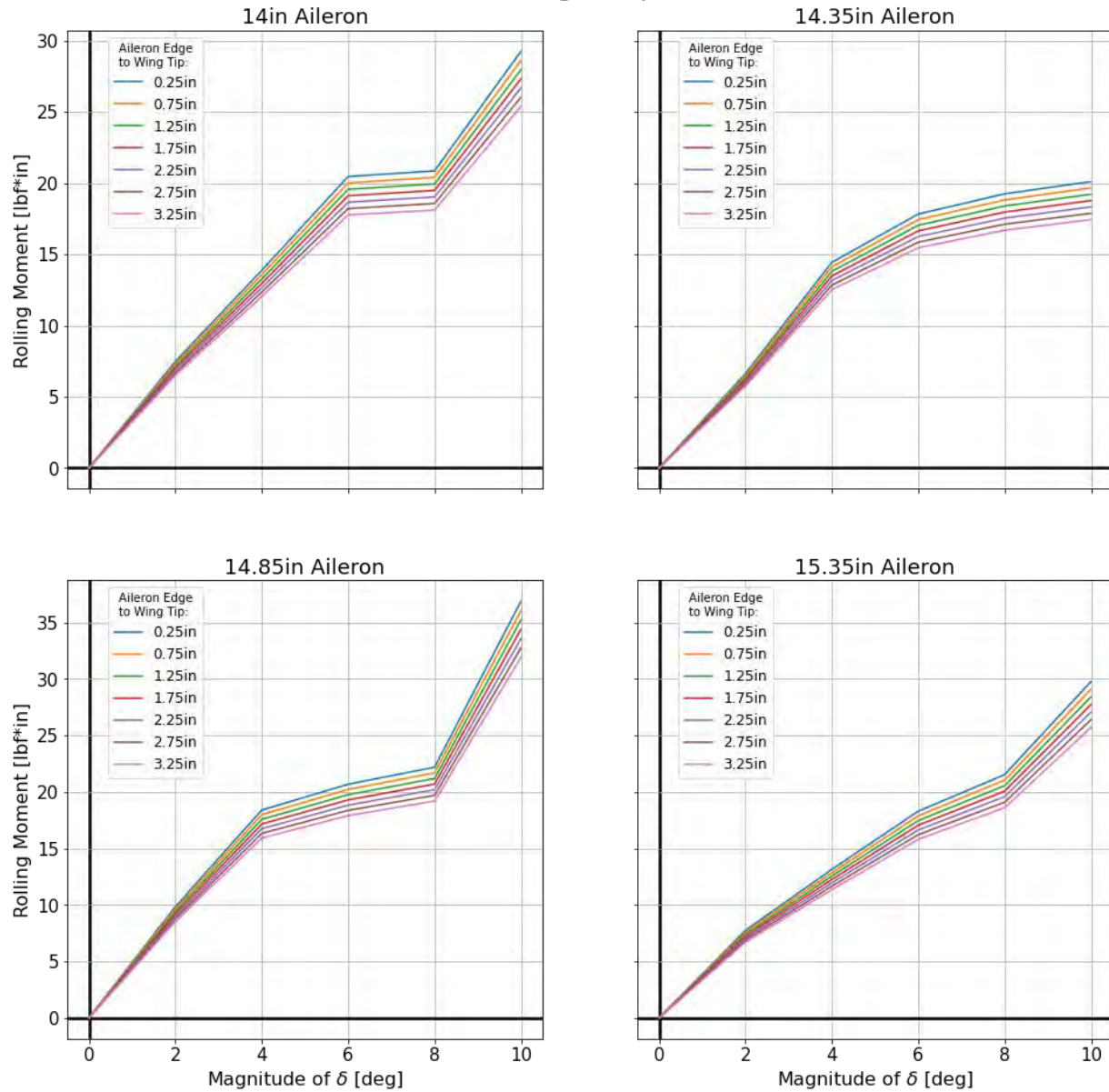
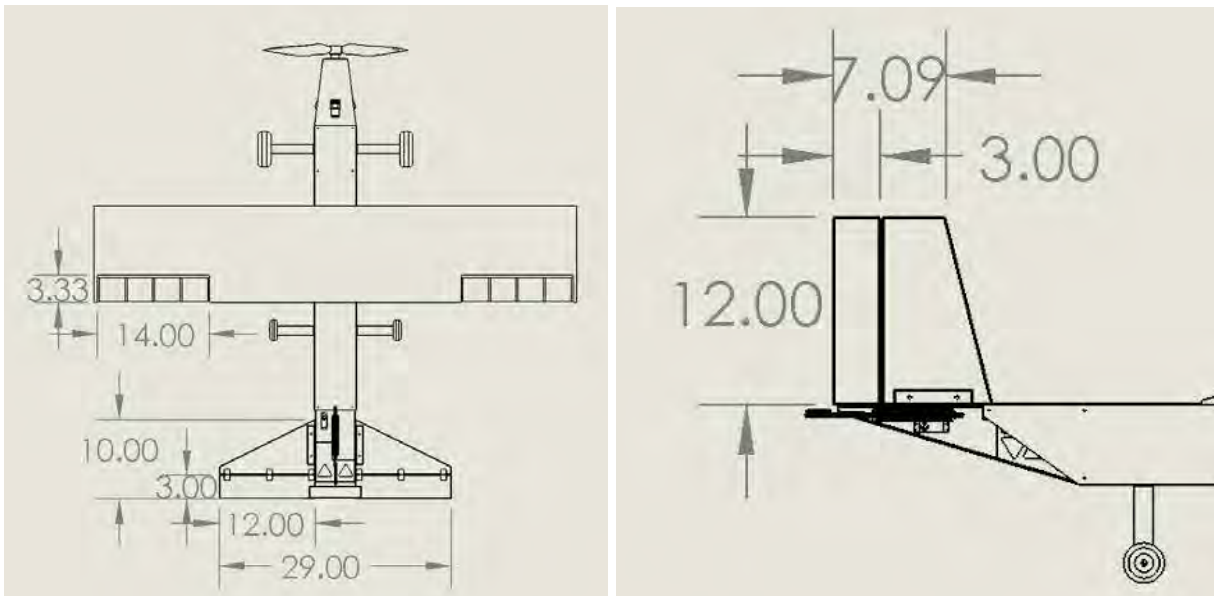


Figure 4.5: Rolling Moment Analysis

Control surface horn locations near the rotation axis were chosen to provide the optimal range of motion for the necessary deflection. Since the horn moves along a perpendicular axis to the control surfaces, the amount of motion needed was much less near the rotation axis. The final control surface dimensions are shown in Figures 4.6A and 4.6B.



Figures 4.6A and 4.6B: Horizontal and Vertical Stabilizer and All Control Surface Dimensions

4.2.5 Servo Torque Sizing

The aircraft has four control surfaces operated by five servos. The servos needed to produce enough torque to deflect the rudder, elevator, and ailerons $\pm 16.5^\circ$, $\pm 8.5^\circ$, and $\pm 8.5^\circ$ respectively, while resisting wind speeds and induced airflow from the propeller slipstream. A SolidWorks CFD study was performed to determine aerodynamic loading on the control surfaces and the required torque for each control surface was calculated. Figure 4.7 shows the results of a torque analysis for an assumed airspeed of 80 ft/s, or the expected cruising speed. A Spektrum A6380 was selected, as its 7.3 kg-cm of torque was sufficient to meet the torque thresholds.

A potential concern was the performance of the elevator at more extreme conditions. The elevator was a single surface that spanned both stabilizers and was in the direct path of induced airflow from the propeller. If high speed flight is combined with full power from the motor, a single servo may not generate enough torque to deflect the elevator and a flight failure could occur. To increase the flight reliability of the aircraft, a second elevator servo was added.

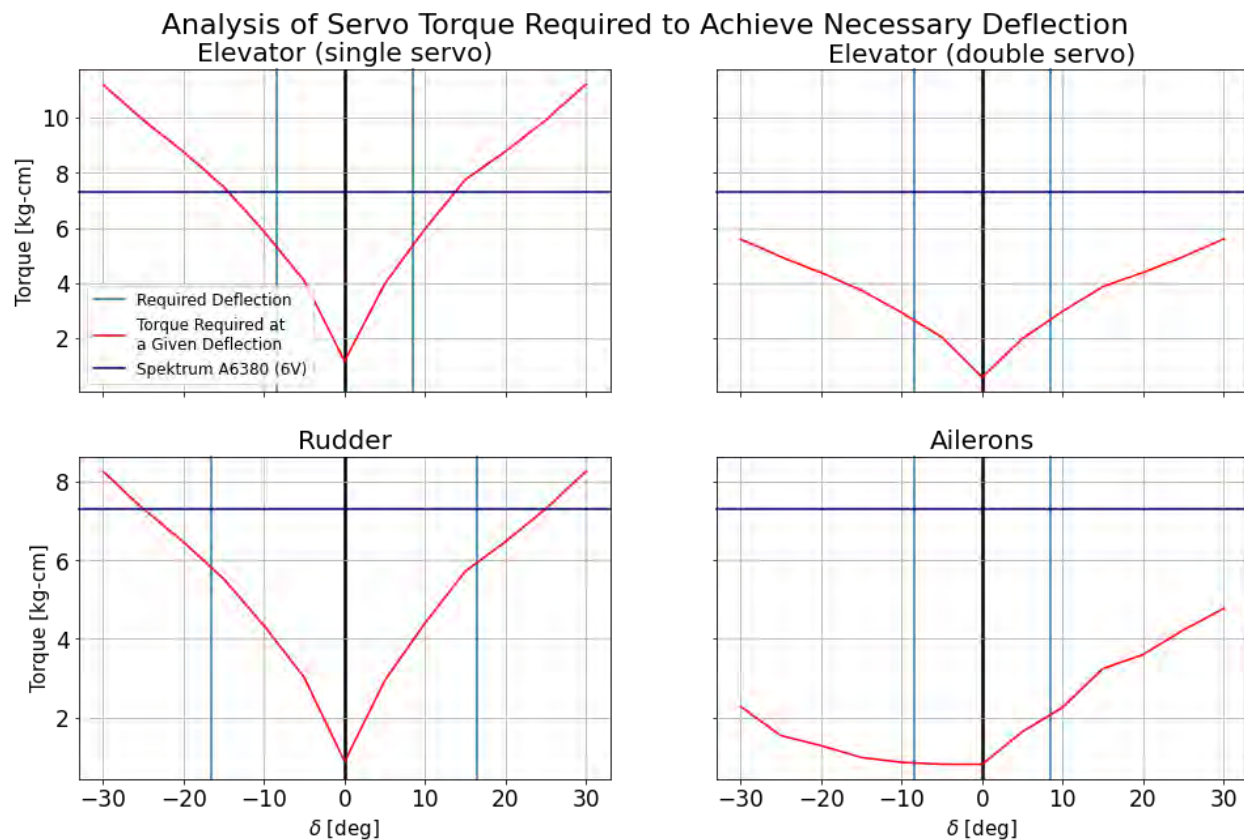


Figure 4.7: Servo Torque Analysis at 80 ft/s

4.2.6 Propulsion Sizing Analysis

The goal of the propulsion system is to provide sufficient thrust for an aircraft to take off within 100 ft. As such, the team set a target takeoff distance of 90 ft. The takeoff velocity was assumed to be 1.1 times the stall speed [6], and kinematic equations were used to solve for the required thrust. The required thrust was calculated to be 11.2 lbf for the worst case scenario weight.

After the required thrust was determined, a motor, propeller, and battery configuration were chosen. A threshold of 100 W per lbf of aircraft weight was chosen for the motor selection based on the required thrust and RC aircraft best practices [7]. Taking into account the extra drag from the deployed sensor, an E-Flite Power 160 motor was selected. This motor provided 125 W/lbf of aircraft weight for the worst case scenario weight, fulfilling the 100 W/lbf requirement while also having extra power to tow the deployed sensor. The Power 160 manual recommended a 20x10 propeller, so an APC 20x10 thin electric propeller was selected. Operating at 50% throttle, the Power 160 was expected to require a continuous current of around 30 A. To complete the sensor mission at this throttle level, the motor required 3000 mAh. A 10S LiPo battery with 4500 mAh was selected as it meets the needs of the motor for the sensor mission with a sizable margin for takeoffs and landings. For the battery's health and safety reasons, LiPo batteries should never be discharged more than 80% of their capacity. Even with this constraint, the power system had 600 mAh to spare during the sensor mission. A ZTW Gecko 120A OPTO electronic speed controller and YEP 20A battery eliminator circuit were selected to exceed the burst 75 amps drawn by the motor and to avoid burnout.

An online thrust calculator was used to verify the motor and propeller achieved the target thrust, and by extension, the target takeoff distance [8, 9]. The calculator estimated the motor and propeller would produce 19 lbf of thrust, which was greater than the required thrust of 11.2 lbf. At full thrust, this selected motor battery combination should takeoff within 70 ft which satisfies the competition requirements.

Not only did the propulsion configuration satisfy the takeoff distance requirement of the aircraft, but it also paired well with the landing gear configuration selected in the conceptual design. The lower rear landing gear increased the distance from the propeller to the ground, which lowered the chances of a propeller strike. A side view of the aircraft is shown in Figure 4.8 to demonstrate this relationship.

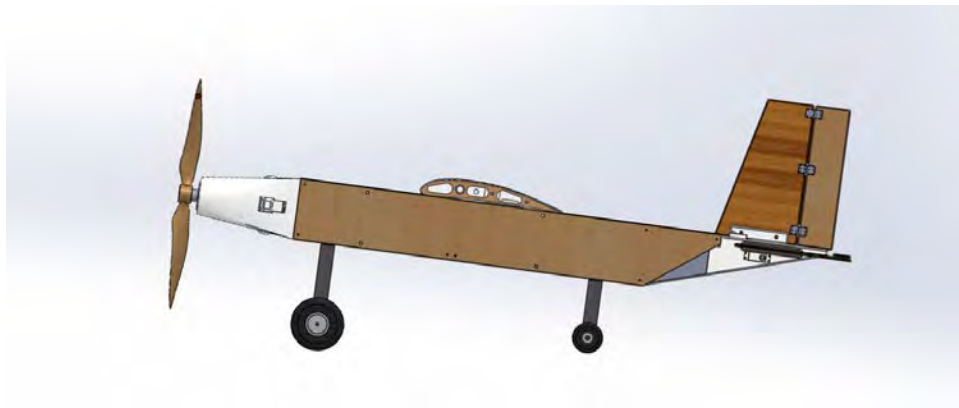


Figure 4.8: Side View of Aircraft Showing Propeller Clearance and Angle of Attack at Take Off

4.2.7 Sensor sizing

The sensor dimensions were selected based on mission requirement and physical limitations of the aircraft. The sensor's internal electronics necessitated a minimum sensor diameter of 1.25 in. Additionally, the minimum 1:4 length to diameter ratio requirement constrained the sensor to a length of at least 6 in. While a longer sensor directly increased sensor mission score, it also reduced cargo storage capacity for the transport mission and added length to the tow cable. A longer sensor would add significant complexity to the deployment, towing, and retrieval of the sensor. Each of these factors translates to decreased mission reliability. As such, a minimal sensor length of 7.32 in was selected to ensure all electronics could be housed inside, the nose cone could be attached, and the dihedral could be added.

The sensor weight also presented a trade off. Sensor weight is directly proportional to the sensor mission score. However, it is inversely related to the plane's load capacity, thereby resulting in a lower delivery mission score. A lighter sensor also improves aircraft flight characteristics, by reducing the center of gravity change during deployment and retrieval. The sensor weight was thus kept to a minimum weight of 0.3 lbf to improve flight dynamics and increase the likelihood of completing the sensor mission successfully.

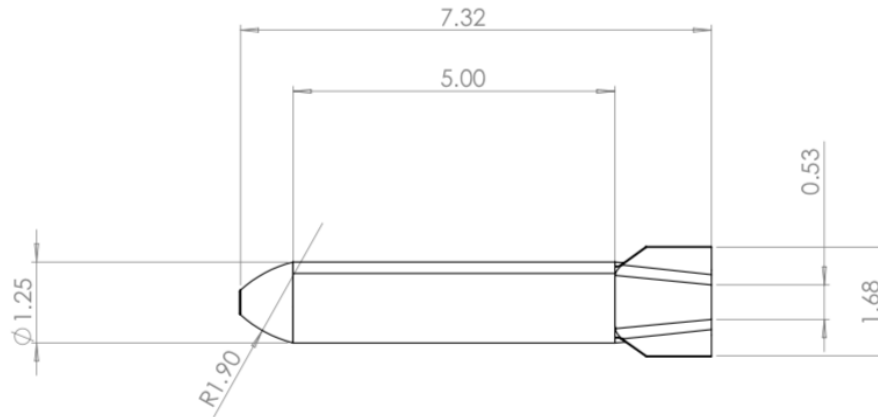


Figure 4.9: Sensor with Dimensions

4.2.8 Sensor Drag Analysis

A comparison CFD analysis was performed to determine the drag caused by the sensor during towing. SolidWorks CFD with default meshing was utilized. The results provided an estimate of the drag produced by the sensor. The sensor coefficient of drag at various speeds was determined and is shown in Figure 4.10. The drag of the sensor was reduced at angles close to the horizontal. Higher airspeeds also reduce sensor drag. In ideal conditions between -2° to 2° of inclination and 120 ft/s, the sensor achieved an optimal coefficient of drag, $= 0.205$. However, it is more likely the aircraft will be cruising around 59.94 ft/s and a sensor angle of attack around 10° , which will result in a $= 0.43$.

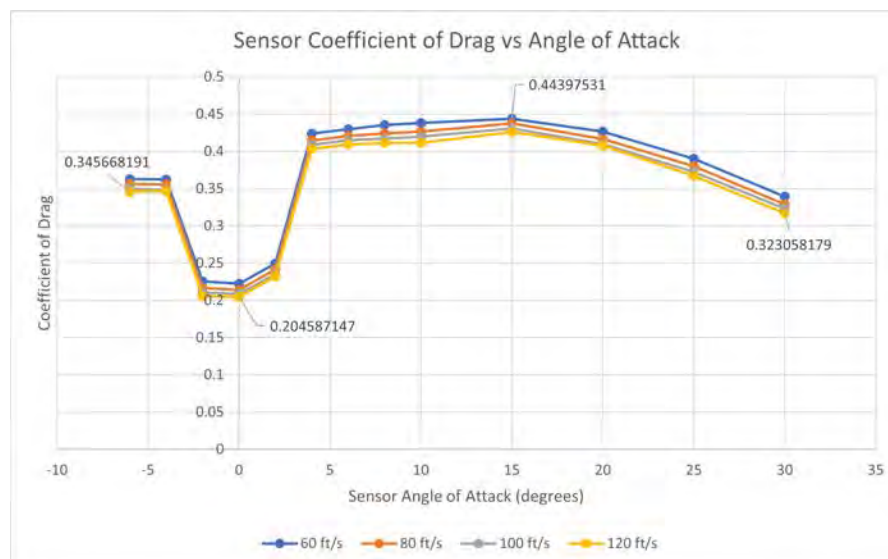


Figure 4.10: Sensor Coefficient of Drag and Angle of Attack

Further CFD analysis was conducted to compare the effect of drag on the plane with and without the sensor being towed. Localized meshing was used to accommodate the various component sizes and improve the reliability of results. The coefficient of drag was determined at an angle of attack ranging between -10° and 30° as well as a velocity of 80 ft/s.

During sensor towing, the total coefficient of drag increased by an average of 20.6%. This is expected to increase the thrust margin by a similar margin, decrease aircraft range, and decrease battery endurance.

4.3 Aircraft Stability

To ensure that the aircraft is effectively controlled in flight, the aircraft's stability was analyzed utilizing tail volume calculations and stability derivatives from AVL, a vortex lattice code developed by Mark Drela [10].

4.3.1 Static Stability Analysis

The tail volume coefficient was an important consideration for control sensitivity. The horizontal tail volume coefficient (V_h) and vertical tail volume coefficient (V_v) equations are shown in Equations 4.4 and 4.5 respectively.

$$V_h = \frac{S_h l_h}{S c} \quad (4.3)$$

$$V_v = \frac{S_v l_v}{S b} \quad (4.4)$$

Typical values for a stable yet maneuverable configuration, typical V_h value range from 0.50 to 0.60 and typical V_v value ranges from 0.05 to 0.06. When the V_h value is lower than the range, the pitch behavior will be sensitive. Similarly, when the V_v value is lower than the range, the yaw behavior will be sensitive [11]. The horizontal and vertical tail volume coefficients were calculated to be 0.51 and 0.058 respectively. These values are typical for an aircraft that is not prone to pitch or yaw sensitivity but can still maneuver effectively. To determine the stability derivatives of the design, a model of the wing and stabilizers were imported into AVL, as shown in Figure 4.11. An evaluation simulated the aircraft taking off during cargo mission. Mission 2 was chosen because the plane would be at its heaviest. The team assumed a 20° climb at takeoff. The stability derivatives from AVL are shown in Table 4.3. The obtained static derivatives showed no signs that the plane would be statically unstable during takeoff.

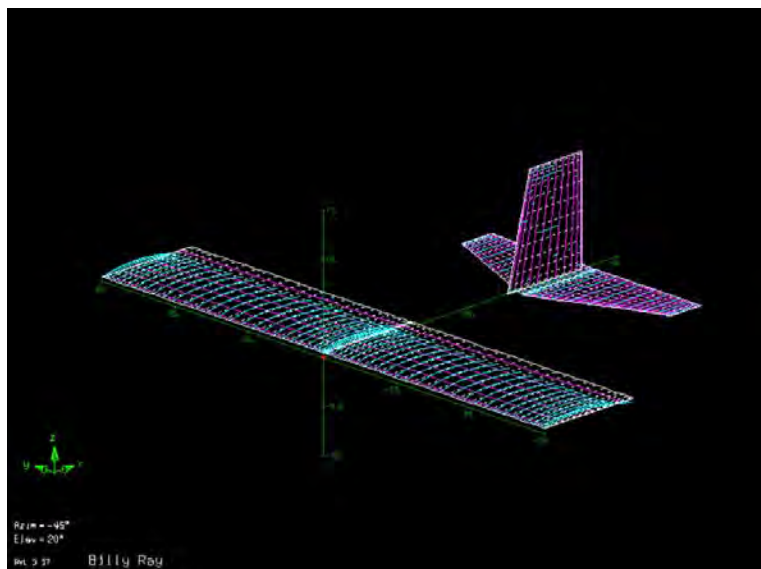


Figure 4.11: AVL Model of Billy Ray Cyrus's Wings and Stabilizers

Table 4.3: Stability Derivatives for Mission 2 at Takeoff (20° Climb)

$C_{L, \alpha}$	3.527	$C_{L, \beta}$	0.000	$C_{L, p}$	0.000	$C_{L, q}$	8.723	$C_{L, r}$	0.432
$C_{m, \alpha}$	-1.092	$C_{m, \beta}$	0.000	$C_{m, p}$	0.000	$C_{m, q}$	-11.802	$C_{m, r}$	0.000
$C_{n, \alpha}$	0.000	$C_{n, \beta}$	0.210	$C_{n, p}$	-0.199	$C_{n, q}$	0.000	$C_{n, r}$	-0.182

4.3.2 Dynamic Stability Analysis

From the AVL analysis of the cargo mission's takeoff, the body-axis derivatives were used to calculate the damping ratio and undamped natural frequency of the aircraft. Five modes were chosen for analysis: short period, phugoid, roll, the Dutch Roll, and spiral. The damping ratio and undamped natural frequencies were estimated using approximated equations [11, 12]. The calculated dynamic characteristics are shown in Table 4.4. Calculations found that the plane would not be stable in a roll or spiral while in a 20° climb. However, during testing, the aircraft handled well and the pilot did not believe dynamic stability was a concern. During sensor deployment, stability would be affected, but the sensor could be deployed slowly to mitigate sudden stability changes and provide ample time for the pilot to adjust .

Table 4.4: Dynamic Stability Characteristics for Cargo Mission at Takeoff

	Short Period	Phugoid	Roll	Dutch Roll	Spiral
Damping Rate (s^{-1})	2.15	0.00873	-0.413	3.20	-0.112
Damping Ratio (-)	0.443	0.00873	-	0.759	-
Undamped Natural Frequency (s^{-1})	2.44	1.88	-	4.32	-

4.4 Predicted Aircraft Performance

This section summarizes the key aerodynamic parameters determined by analyses conducted for the aircraft under different mission configurations.

Table 4.5: Predicted Preliminary Design Aircraft Performance

Performance Parameter	Staging Flight	Delivery Flight	Sensor Flight
Cl_{max}	1.67	1.67	1.67
Cl_{cruise}	0.81	0.81	0.81
Weight[lbf]	17	20	17.3
e	0.93	0.93	1.0
Cd_0	0.085	0.085	0.1025
$(L/D)_{max}$	82	82	82
$(L/D)_{cruise}$	62	62	62
V_{cruise} [ft/s]	59.41	64.44	59.94
V_{stall} [ft/s]	41.80	45.36	42.19
W/S [lbf/ft ²]	3.4	4	3.46
Mission Score	1	1.48	2.008

5. Detail Design

The detailed design was an iterative process, where the exact specifications of each component were defined, analyzed for performance characteristics, and re-defined to improve performance. The final system architecture of the aircraft with dimensional parameters, sub system interfaces, and the detailed design of each sub system is presented. Aircraft structural characteristics were analyzed using FEA and the results show that loads do not exceed critical levels during flight. Final theoretical values for weight, mass, flight, and mission performance are documented. A drawing package includes a 3-view, exploded aircraft view, control system layout, sensor and shipping container, and sensor deployment and retrieval system drawings of the final design.

5.1 Dimensional Parameters

The final dimensional parameters are listed in Table 5.1. After thorough computational analysis, the final design was selected to provide high reliability and while effectively accomplishing the mission requirements.

Tables 5.1: Dimensional Parameters of Aircraft

Overall Dimensions		Wing Dimensions	
Length (in)	57.24	Span (in)	60
L.E. X-Location (in)	18.89	Mean Chord (in)	12
C. G. X-Location (in)	22.25	Aspect Ratio	5
Static Margin (% MAC)	25.9	Area (ft ²)	5

Vertical Tail Dimensions		Horizontal Tail Dimensions	
Height (in)	12	Span (in)	29
Mean Chord (in)	8.59	Mean Chord (in)	7.43
L.E. X-Location (in)	45.50	L.E. X-Location (in)	47.35

5.2 Sub System Architecture, Integration, and Dimensions

5.2.1 Sub System Integration and Architecture - Wing

The final wing design was composed of one structural spar, two alignment spars, structural ribs, mounting ribs, servo mounting plates, and ailerons. Plywood ribs slid onto the carbon fiber spars and were fixed in place with epoxy. Servo mounting plates were mounted between the ribs, directly in front of the ailerons, to house the aileron servos. Ailerons were composed of plywood ribs wrapped in a balsa skin and duct tape, and utilized the rear alignment spar as a guide pin to rotate. Each mounting rib had two threaded rods used to attach the wing to the fuselage mounting plate. The bolts were secured with nuts. An assembly of the wing is shown in Figure 5.1.

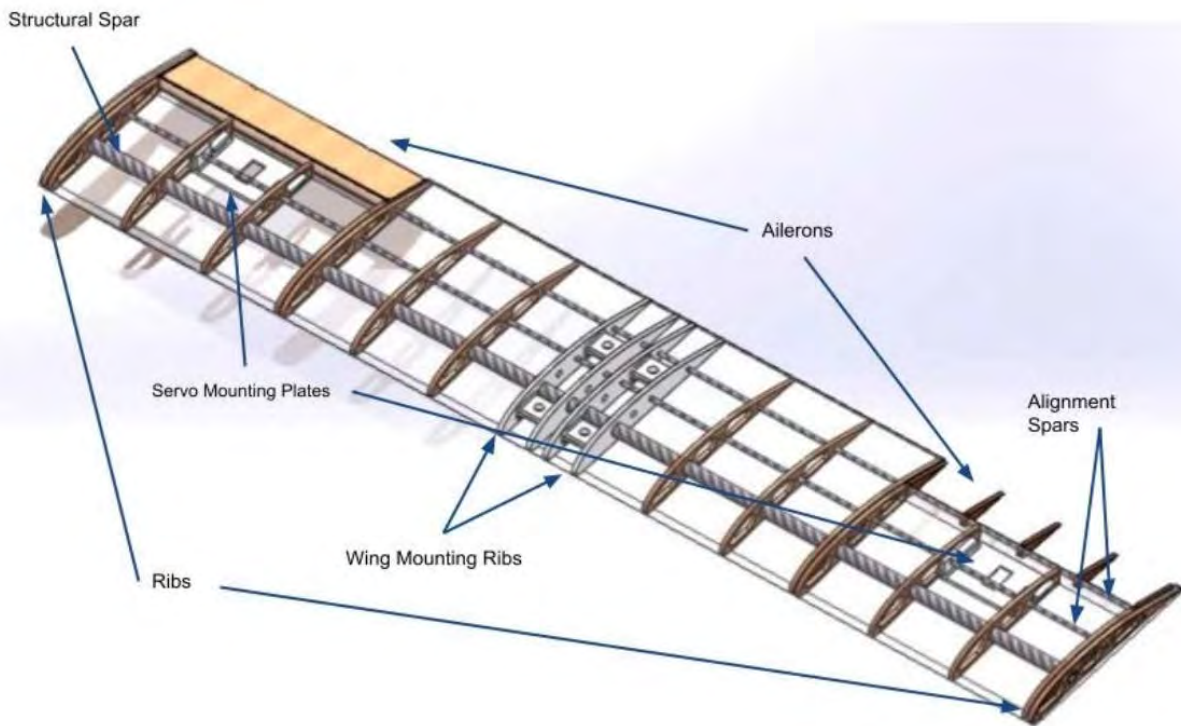


Figure 5.1. Wing Design with Key Components Labeled

5.2.2 Nose Cone Integration and Architecture

The nose cone mated with extruded angle stringers on the fuselage, and attached using eight screws and nuts. The motor mounted to the inner shell of the nose cone using bolts. A section view showing the internal cavity, motor, propeller, and ESC is shown in Figure 5.2.

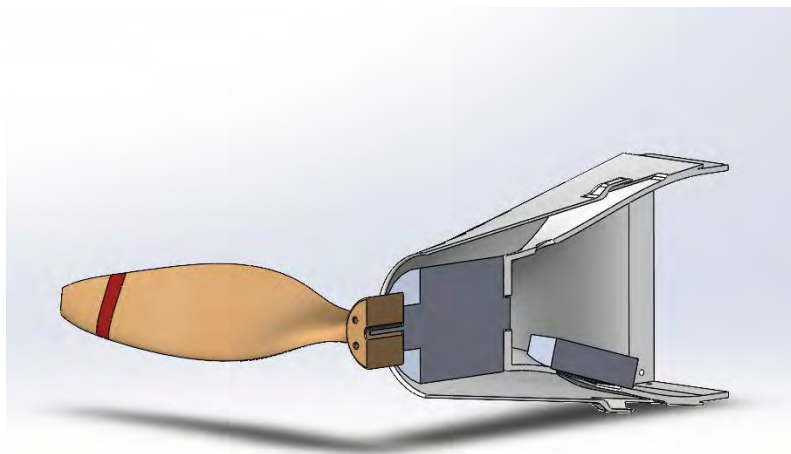


Figure 5.2: Section View of Nose Cone Assembly

5.2.3 Empennage Integration and Architecture

The tail cone was composed of two separate ABS plastic sections. The front section was mated with the extruded angle stringers on the fuselage, and attached using screws and nuts. The rear section was mated with the front section and was secured with screws and nuts. The aft tail cone section contained three sandwich slots that attached to the stabilizers with bolts and nuts. For each stabilizer, three plastic hinges secured the balsa control surfaces. Cutouts in both sections were created for the control surface servos and cargo door. An assembly of the empennage is shown in Figure 5.3.

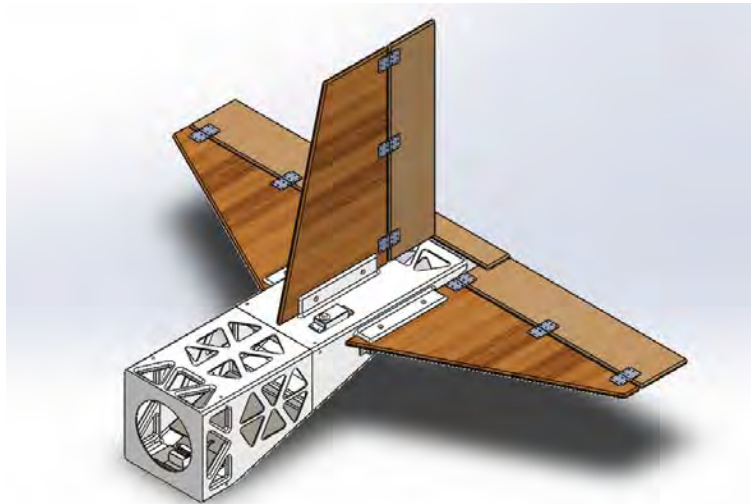


Figure 5.3: Isometric View of Empennage Assembly

5.2.4 Fuselage Integration and Architecture

Aluminum extruded angles, used as stringers, comprised the main structure of the fuselage. An aluminum wing mounting plate was epoxied to the top extruded angles. The plate had multiple sets of holes which allowed the wing to mount at different locations along the aircraft's longitudinal axis, depending on the mission. A series of formers were epoxied to the inside edges of the stringers, with the front former also acting as a battery basket. The nose cone and empennage acted as the front and rear bulkheads of the fuselage. Carbon fiber landing gear brackets were bolted to the bottom extruded angles and secured with nuts. The skin of the fuselage was composed of four balsa sheets. The fuselage assembly is shown in Figure 5.4.

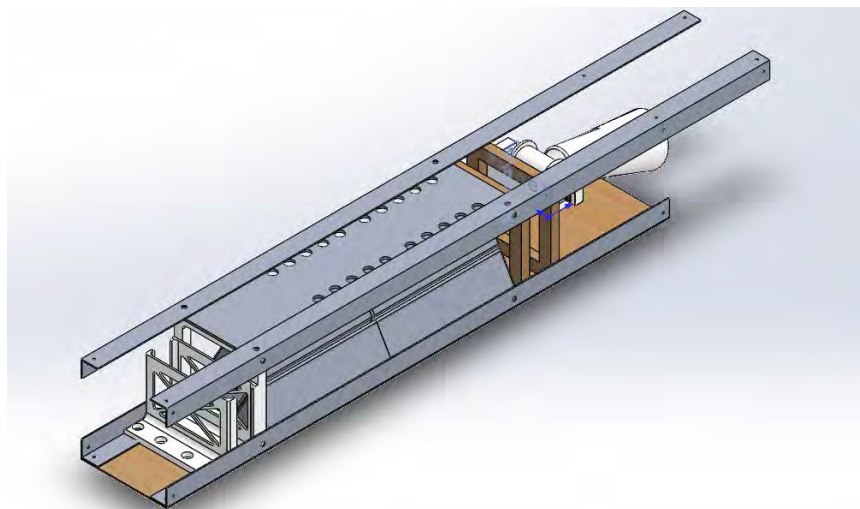


Figure 5.4: Isometric View of Fuselage Internals Without Skin

5.2.5 Controls Integration and Architecture

The control system consisted of the following components: a receiver, an ESC, a BEC, servos, Arduinos, and batteries. The receiver and BEC were duct taped to level interior surfaces inside the nose cone. The ESC mounted to a cutout in the nose cone that provided airflow for convective cooling. The receiver antennas were placed orthogonal to each other and avoided the metal extruded angles to allow for the best receiver performance. The batteries were placed in the battery basket and secured with velcro straps.

The control surface servos were secured with screws or zip ties to the servo hole cutouts in the empennage and wing servo mounting plates. For the aileron servos, the wing rib structure allowed wiring to be threaded from the fuselage wing mounting plate through the wing to connect with the servos. The servos and transmitter were set up to displace the ailerons ± 0.43 in, the elevators ± 0.43 in, and the rudder ± 0.87 in at the trailing edges. One of the elevator servos required an inverter to match the direction of the other elevator servo when rotating. This inverter was installed inline with the servo. The controls layout is shown on Page 3 of the drawing package.

5.2.6 Special Mission Components Integration and Architecture

5.2.6.1 Sensor Integration and Architecture

The sensor body was composed of two main components: the electronics tray and the outer sleeve, as shown above in Figure 5.5. The outer sleeve was a thin tube that has a length of 6.5 in, a diameter of 1.25 in, and dihedral fins. The sleeve acted as a protective housing for the electronics and provided aerodynamic stability for the sensor during flight. The outer sleeve slid over the tray, which allowed for easy electronics access. The electronics tray secured all the hardware including LED lights, battery, and microcontroller. The tray was attached to the nose cone. An audio cable was connected with the nose to tow the sensor and receive signals from the aircraft. The sensor weighed 0.206 lbf, with the bulk of the mass concentrated at the lower front of the sensor. This provided the sensor with stability during towing as the center of gravity was located in front of the center of pressure.

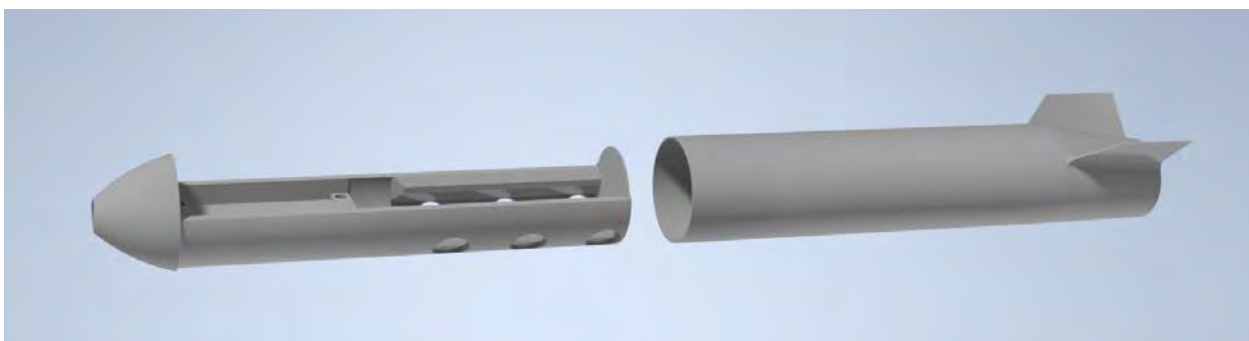


Figure 5.5: Sensor 3D Printed Components

The electronics of the sensor included a microcontroller, audio port, LiPo battery, six MOSFETs, and six LEDs. Custom circuitry was developed, as no commercial lighting system was suited for the mission application. Six 3W LED diodes were used for the sensor lights. The diodes have a wide 180° viewing angle and allow for consistent visibility during sensor deployment. Green colored lights were selected to contrast with the blue or gray sky. Each green LED provided

160 lumens at a maximum rated 500 mA draw. The system is powered by a 650 mAh, 3.4 V LiPo battery. It supplied at least 15 min of runtime with the LEDs running at maximum current draw. The microcontroller, an Adafruit Feather M0 board, controls each LED individually and a MOSFET driver circuit powers each LED at maximum brightness. The LEDs were soldered to the MOSFET heatsinks to prevent diminishing power from overheating. The Feather microcontroller was programmed to switch each LED on one at a time in sequence when an input signal had been received from the audio towing cable. A schematic of the electronics is shown in Figure 5.6.

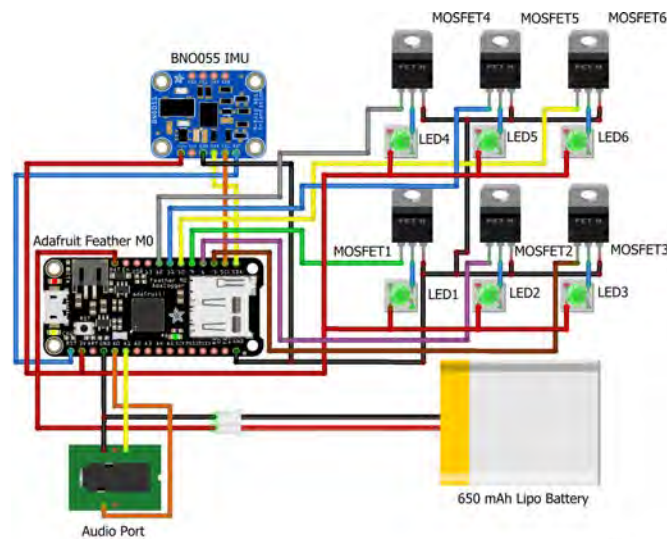


Figure 5.6: Sensor Electronics Schematic

5.2.6.2 Sensor Deployment and Retrieval Mechanism Integration and Architecture

The deployment and retrieval mechanism was composed of a cargo door, cargo door servo, rotational corkscrew, sensor docking station, winch, winch servo, and audio towing cable. The cargo door was glued into the front tail cone cutout. A servo was glued in front of the cargo door and utilized a rotating corkscrew to open and close the door. The sensor docking station was zip tied to the top stringers. A winch was epoxied to the rear former and connected with a servo to deploy, tow, and retrieve the sensor from the sensor docking station. The winch stored up to a 84 in audio tow cable. The audio tow cable is connected to an arduino, wrapped around the winch, and connected in the nose of the sensor. As the winch was turned, the cable unwrapped (or wrapped) to deploy (or retrieve) the sensor. The audio cable transmitted signals from the receiver, through the arduino, to the sensor to start the lighting sequence. Arduinos were used to augment the winch and cargo door servos to rotate continuously. The servos, arduinos, and the tow cable were wired to and received commands from the receiver.

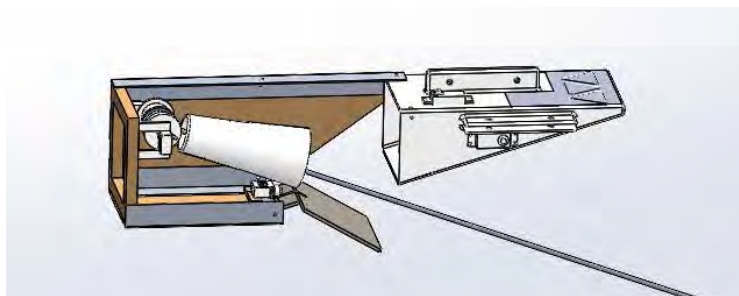


Figure 5.7: Sensor Deployment and Retrieval Mechanism

5.2.6.3 Sensor Shipping Containers, Simulator Shipping Containers, and Cargo Hold Integration and Architecture

The shipping container was composed of a 3D printed, hollow triangular prism and sleeve that covered the sensor slot, as shown in Figure 5.8. The container was packed with foam to protect the sensor during drop shock events. The simulator shipping containers were also 3D printed, but instead of a sensor, they were filled with sand to match the weight of the shipping container with the sensor inside. The sleeves on both types of containers were secured with duct tape. During the delivery flight, shipping containers were loaded beneath the wing mounting plate to keep the CG beneath the center of lift, and were secured with duct tape.

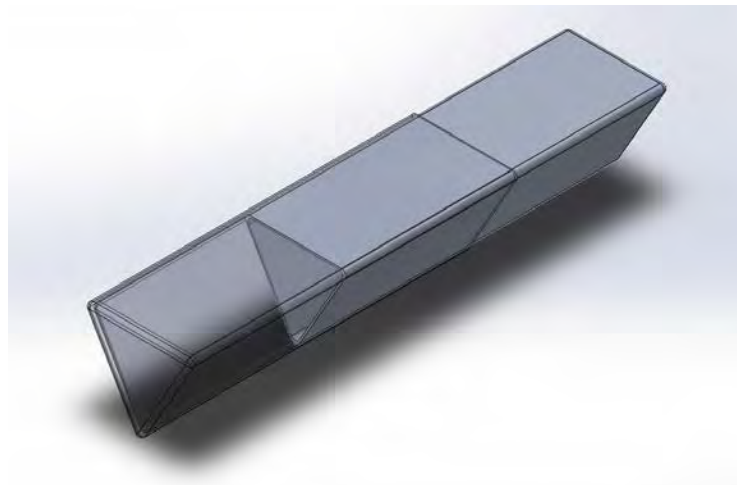
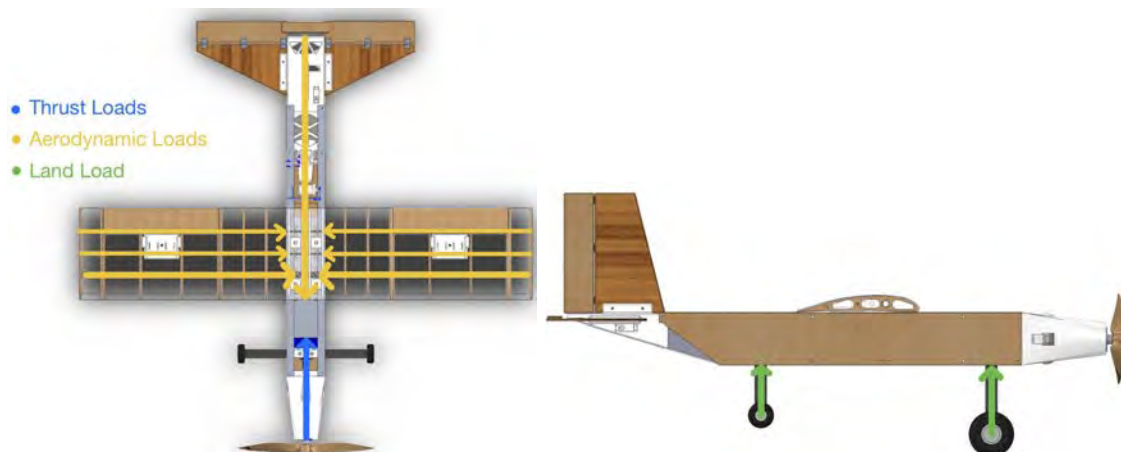


Figure 5.8: Shipping Container with Transparent Sleeve

5.3 Structural Characteristics and Capabilities

5.3.1 Aircraft Load Pathing

The aircraft was subjected to three primary loads: thrust, aerodynamic, and landing. Thrust loads originated from the propeller and extended back into the fuselage. The aerodynamic loads were caused by wing lift, drag, and moments, which primarily affected the wings. Landing loads were experienced directly on the landing gear bracket when the aircraft touched down. Figures 5.9A and 5.9B illustrate the distribution of the loads on the aircraft.



Figures 5.9A and 5.9B: Top View and Side View Showing Loads

5.3.2 Structural Characteristics - Wing

This section presented the structural capabilities of the wing while highlighting the aerodynamic loading of the wing and rib geometry performance under loading. Finite element structural analysis was performed on several different rib designs to determine an optimal balance between rigidity and weight. Cutout holes were added to decrease the weight of the ribs. The top three design styles and the results of the analysis is shown in the following Figures 5.10. The stress for all designs was well below the critical loading. As such, Design III was selected to minimize weight.

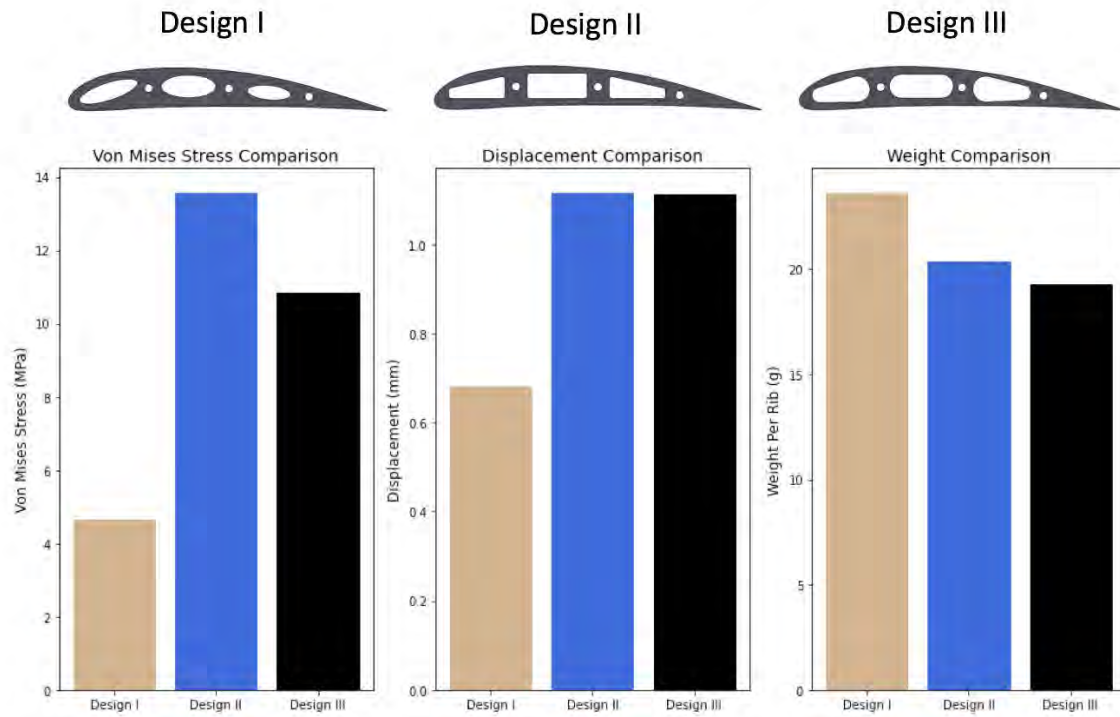


Figure 5.10: Wing Rib Cutouts Designs: FEA and Weight Comparison

The next important structural wing consideration was the mounting ribs. The mounting ribs would take large loads due to aerodynamic loading on the wing. The mounting ribs are secured to the fuselage attachment plate using a threaded rod. Two structural cases were considered. In the first, the platform for the threaded rod could fail while supporting the weight of the aircraft. In the second, the wing attempts to shear along the fuselage. These models informed the FEA loading. In the aerodynamic force model, a force, equivalent to the worst case weight, was applied along the top of the mounting bolt connection supports as shown in Figure 5.11. This model simulated the mounting ribs supporting the plane during flight. In the shear model, forces equal to the worst case weight were concentrated within the bolt attachment holes. Of the two models, the aerodynamic force produced higher stress and thus was the basis for determining our safety factor. With a safety factor of 13.3, the mounting ribs would not yield during loading.

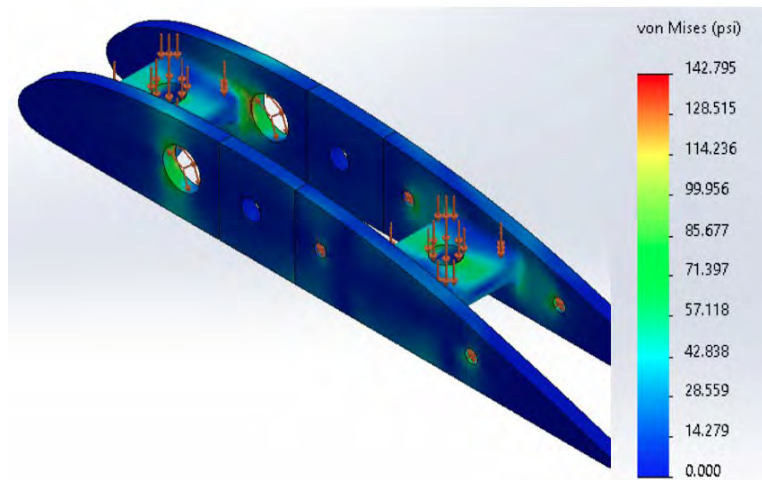


Figure 5.11: Mounting Rib Expected von Mises Stress

5.3.3 Structural Characteristics - Nose Cone

The nose cone was constructed of a double-lofted cylindrical shape, which provided a rigid support for the motor. The design was intended to dampen and transfer structural loads from the motor to the main body of the fuselage. The motor mounting cylinder could withstand torsion in excess of 7.5 ft-lbf. This was below the expected torque of 2.5 ft-lbf produced by the motor operating at maximum RPM.

5.3.4 Structural Characteristics - Fuselage

In a semi-monocoque structure, the skin handles shear and torsional loads, the stringers handle bending and axial loads, and the formers prevent buckling. To ensure structural integrity of the wing attachment piece along the stringers, FEA was conducted. An enveloping lift load of 100 lbf was applied to the extruded angle wing attachment points assuming no shear stress is picked up by the skin. Even with this highly unexpected boundary case, the von Mises stress acting on the aluminum was still well below its tensile endurance limit. This is shown in Figure 5.12.

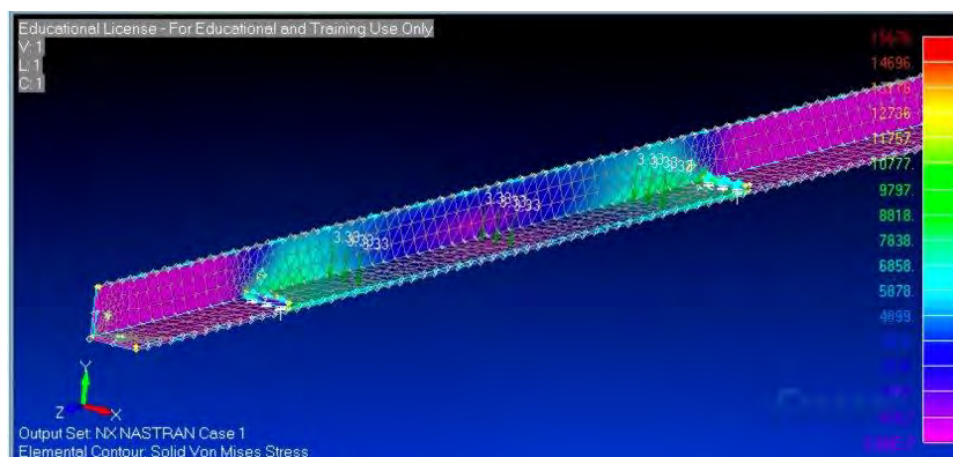


Figure 5.12: von Mises stress on stringer from FEA

Additionally, with the balsa skin, hand calculations found that the fuselage can handle a torsional load close to 2200 ft-lbf, which was well above expected enveloping air and ground loads.

5.3.5 Structural Characteristics - Empennage

The empennage would be subjected to aerodynamic and inertial loads during flight. The tail cone surface had triangular holes cut to create a system of trusses and reduce total weight. An FEA was conducted to determine if the design was structurally sound, and is shown in Figure 5.13. The loads were applied to the stabilizer attachment points to simulate a dynamic pressure on the stabilizers. These loads were higher than what the team would expect during flight to test the effectiveness of the design. The results of the analysis showed that the stress and the displacement were minimal, indicating the design would be structurally sound during flight.

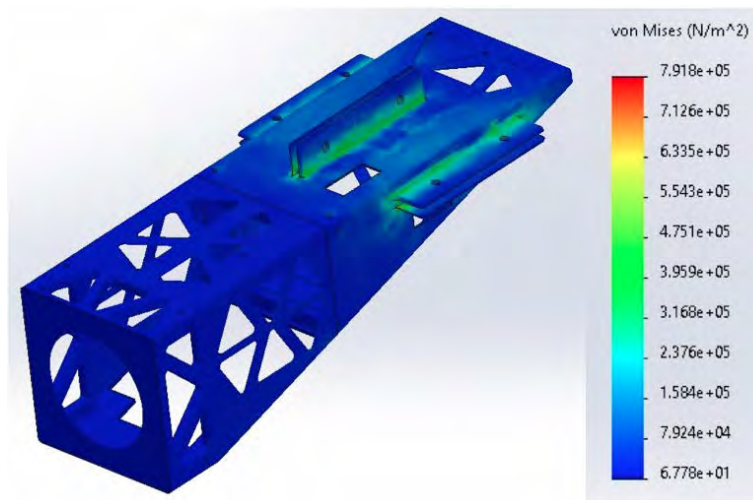
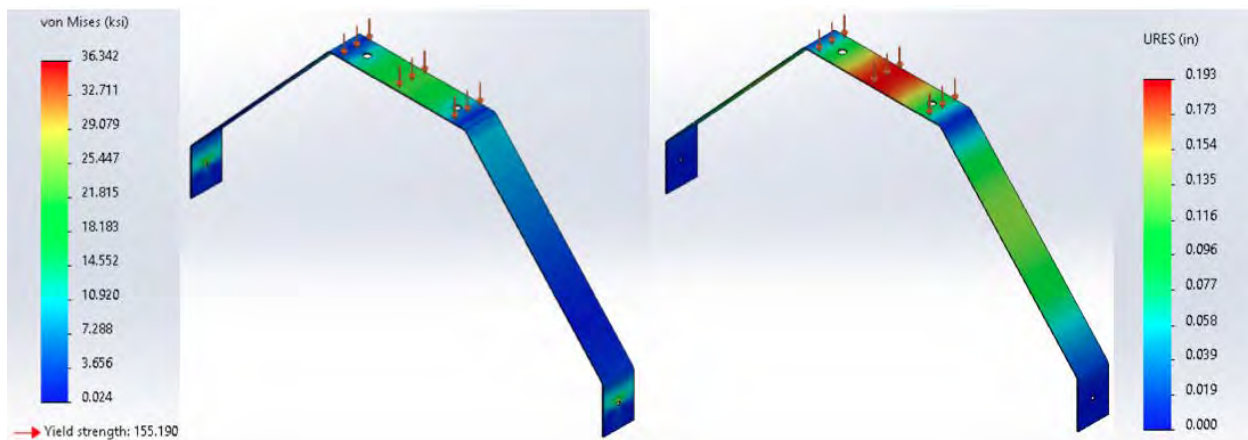


Figure 5.13: Empennage Expected von Mises Stress

5.3.6 Structural Characteristics - Landing Gear

The landing gear was U-shaped and composed of a carbon fiber woven structure. This material made the landing gear durable under large amounts of stress and strain. Using FEA, loads were applied to the top of the horizontal bar at the connection points to the fuselage. Testing showed some deformation under the expected landing loads, but not enough to significantly damage the structural capabilities of the gear. Figure 5.14 shows the FEA analysis including von Mises stress and displacement.



Figures 5.14A and 5.14B: FEA Analysis of the Landing Gear

5.3.7 Structural Characteristics - Shipping Containers

The shipping containers were studied to determine how they would perform during a drop shock event. An FEA was run on three sides of the shipping container: the rectangular face, triangular face, and rounded corner. Stress tended to be concentrated in the center and towards both ends of the rectangular face. The maximum stress endured out of all the faces was about 0.8978 ksi. This is significantly less than the range of the yield strength for the ABS material which is 1.89-9.43 ksi. Due to this difference, the team can conclude that the container will not break on impact when dropped from 10 in. While this does not verify the sensor will be protected from drop shock events, it does verify the containers should be rigid enough to withstand the drop.

5.3.8 Flight Envelope

Several assumptions were made to generate the velocity versus load factor diagrams shown in Figure 5.15. First, it was assumed that the aircraft was flying at ISA+0 conditions at 200 ft MSL, approximately the altitude of where the competition flight will occur in Fairfax County, VA. The aircraft was assumed to weigh 13 lbf for the staging flight, 16 lbf for the delivery flight, and 13.3 lbf for the sensor flight. The stall speeds were determined using the St. CYR 24 maximum coefficient of lift values. The maximum load factors were assumed to be +2.23 and -1.25. The aircraft's cruise velocity is approximately 51.96 ft/s during the staging flight, 57.64 ft/s during the delivery flight, and 52.55 for the sensor flight.

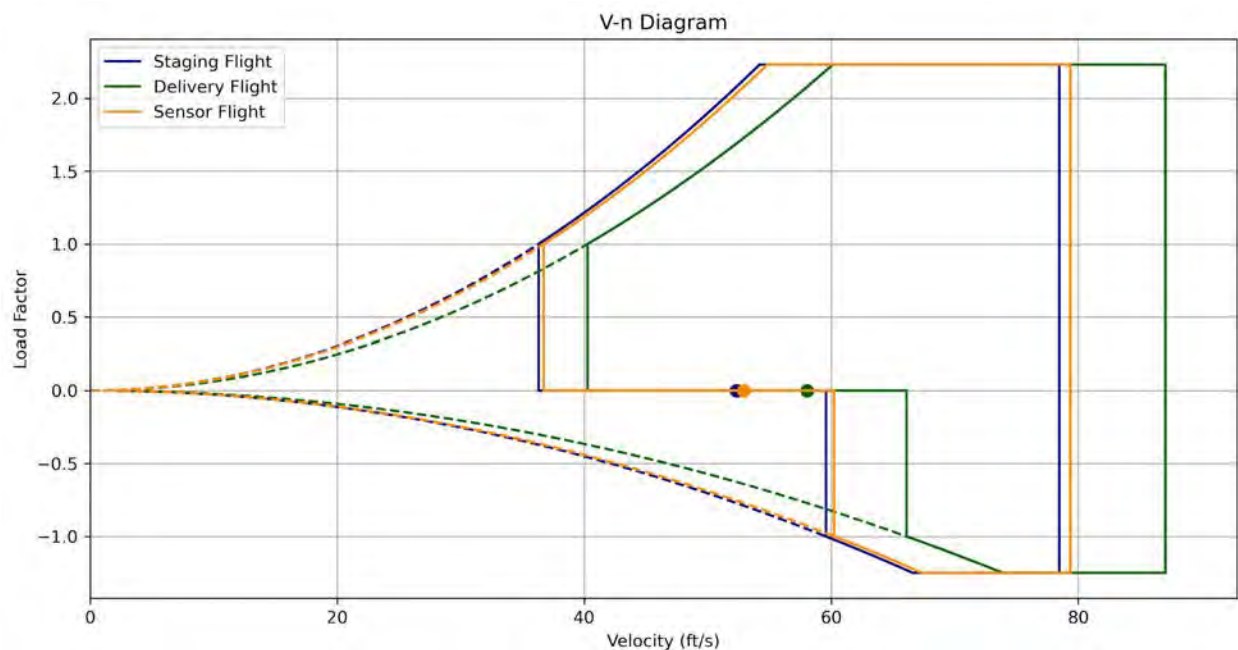


Figure 5.15: V-n Diagram for Staging, Delivery, and Sensor Flights

5.4 Weight and Mass Balance

An internal requirement for the team is that the aircraft's CG shall be located between 25-30 %MAC. This is critical for maintaining control of the aircraft during flight, as a center of gravity outside of the range would make the aircraft nose or tail heavy and difficult to control when maneuvering. To verify this requirement was met, the weight, distance from the front of the fuselage, and moment arm was recorded for each component within the CAD model. The center of gravity was then calculated and verified on the prototype aircraft. The weight and mass balance table is shown below.

Table 5.2: Aircraft Final Weight and Mass

Category	Component	Weight (lbf)	X from Front Fuselage (in)	Moment (lbf-in)
Staging Flight				
Structure	Fuselage (stringers, formers, and skin)	3.14	14.45	45.37
	Wing	3.24	13.68	44.32
	Tail	2.16	38.27	82.66
	Aileron Servos	0.17	17.07	2.9
	Rudder and Elevator Servos	0.28	38.63	10.82
	Front Landing Gear	1.8	3	5.4
	Rear Landing Gear	0.37	25.88	9.58
	Sensor Winch, Dock and Door	0.31	26.2	8.12
Propulsion	Nose Cone+Esc	1.1	-2.97	-3.27
	Motor	1.25	-7.3	-9.13
	Battery Box	0.9	-4.48	-4.03
	Propellor	0.04	-9.61	-0.38
Delivery Flight				
Delivery Flight Components	Simulated Shipping Containers	0.195 (x8)	13.65	21.29
	Cargo	0.3 (x8)	13.81	33.14
Sensor Flight				
Sensor Flight Components	Sensor	0.3	26.2	7.86
	Sensor Deployed	0.3	82.58	24.774
Center of Gravity				
Mission	Staging	Delivery		Sensor (Stowed/ Deployed)
X From Front Fuselage (in)	13.03	13.11		13.27/13.97

5.5 Flight and Mission Performance

Given the analysis conducted and the expected high flight reliability of the Cyrus design, the team expects to complete the staging and delivery flight with relative ease, while the sensor mission will be more challenging. The sensor flight requires the aircraft to be flown to maximize aerodynamic efficiency, and by extension range and battery endurance, to complete the mission. As such, a skilled RC test pilot will be utilized by the team to conduct all flights. The final design's predicted flight and mission performance is shown below in Table 5.3.

Table 5.3: Predicted Flight and Mission Performance

Parameter	Mission 1	Mission 2	Mission 3
Weight (lbf)	13	16	13.3
W/S (lbf/ft ²)	2.6	3.2	2.66
Takeoff Distance (ft)	57.98	87.83	60.65
Climb Rate (ft/s)	7.68	8.52	7.76
Turn Radius (ft)	100	100	100
Turning Rate (deg/s)	29.77	33.03	30.11
L/D_{\max}	82	82	82
L/D_{cruise}	62	62	62
Cl_{\max}	1.67	1.67	1.67
Cl_{cruise}	0.81	0.81	0.81
V_{cruise} [ft/s]	51.96	57.64	52.55
V_{stall} [ft/s]	36.2	40.1	36.6
e	0.93	0.93	1.0
Cd_0	0.085	0.085	0.1025
Lap Time Estimate (s)	68.7	61.94	67.95
Scoring	1	1.43	2.007

5.6 Drawing Package

The drawing package is 5 pages and consists of the following:

- A 3-view drawing
- A detailed view of the structural arrangement
- The control system's layout
- A detailed drawing of the payload
- A detailed drawing of the deployment system

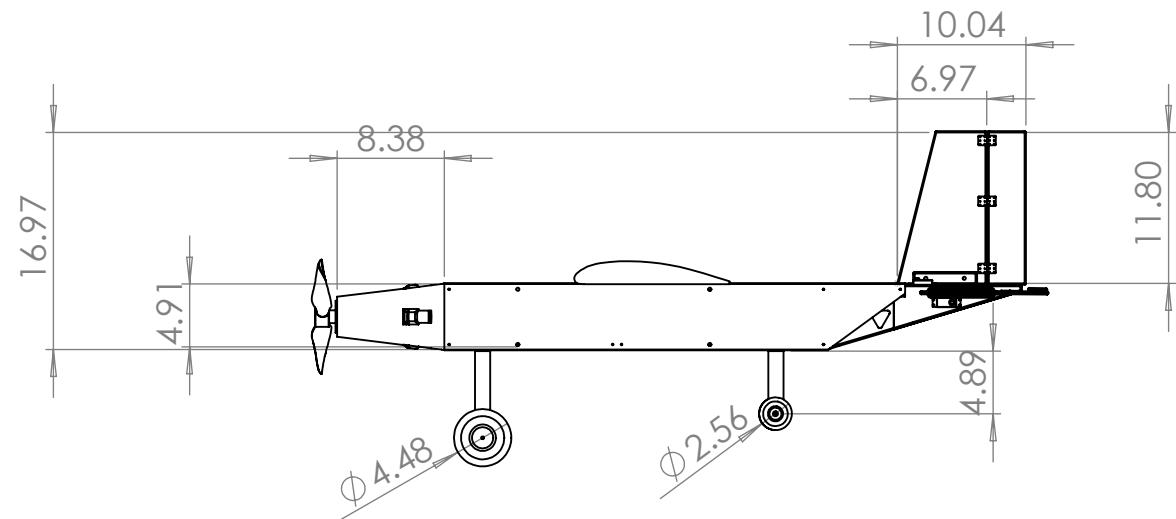
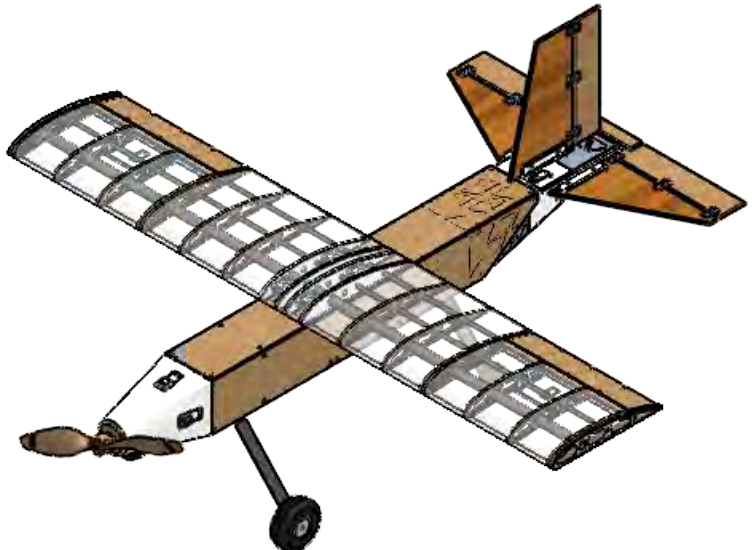
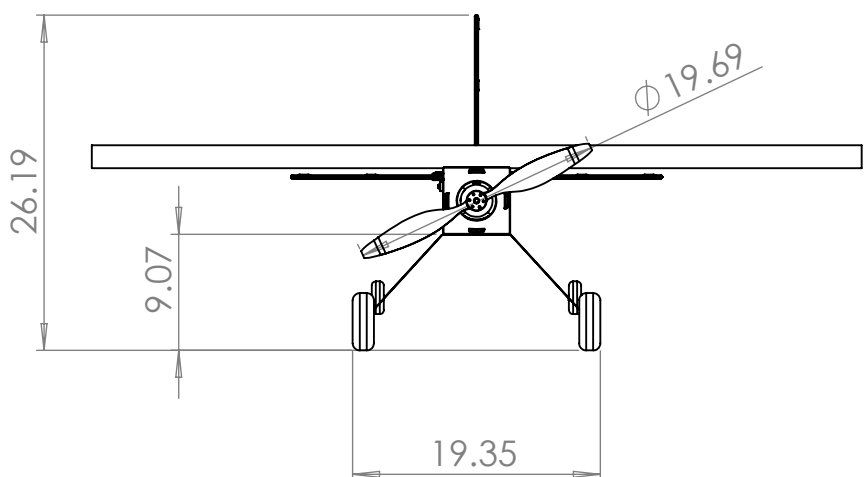
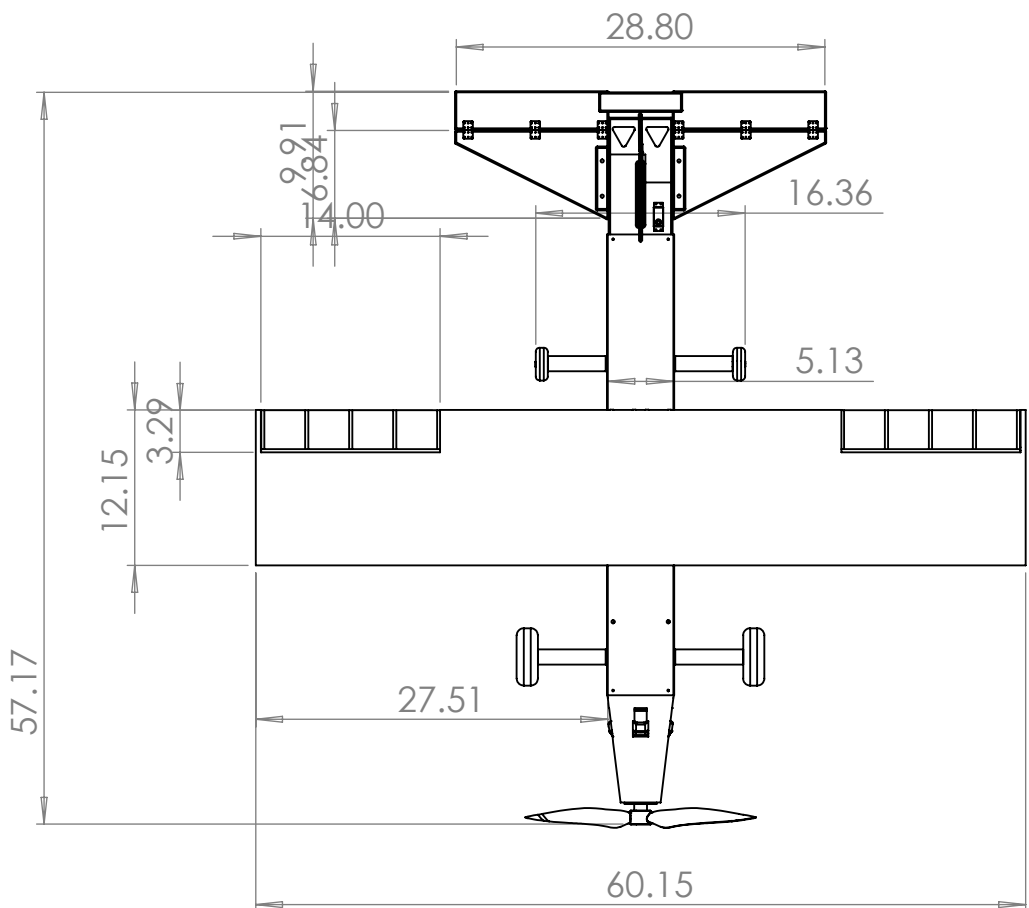
4 3 2 1

B

B

A

A



Note: Units are in inches

George Washington University		
Billy Ray Cyrus		
Drawn By: Matthieu Andre	TITLE: 3 View Drawing	
SCALE: 1:15	02/19/2021	SHEET 1 OF 5

4

3

2

1

Item No.	Part Name	Qty.
1	Propeller	1
2	Motor	1
3	Nose Cone	1
4	Front Landing Gear Support	1
5	Front Wheels	2
6	Fuselage	1
7	Rear Landing Gear Support	1
8	Rear Wheels	2
9	Tail Cone Front	1
10	Tail Cone Back	1
11	Horizontal Stabilizers	2
12	Elevator	1
13	Rudder	1
14	Vertical Stabilizer	1
15	Ailerons	2
16	Wing	1

An exploded view diagram of a model airplane. The diagram shows the following components: 1. Propeller (brown, 3-bladed), 2. Motor (grey, cylindrical), 3. Nose Cone (white, conical), 4. Front Landing Gear Support (black, L-shaped), 5. Front Wheels (black, two), 6. Fuselage (brown, long rectangular body), 7. Rear Landing Gear Support (black, L-shaped), 8. Rear Wheels (black, two), 9. Tail Cone Front (white, conical), 10. Tail Cone Back (white, conical), 11. Horizontal Stabilizers (brown, two), 12. Elevator (brown, single), 13. Rudder (brown, single), 14. Vertical Stabilizer (brown, single), 15. Ailerons (brown, two), 16. Wing (brown, two). The diagram is an exploded view showing the assembly of the airplane. The parts are numbered 1 through 16, corresponding to the parts list. The diagram is oriented horizontally, with the nose of the airplane pointing to the left. The wings are shown in a slightly raised position. The landing gear is shown in a retracted position. The tail section is shown in a slightly offset position. The diagram is a technical drawing, likely created using CAD software.

George Washington University

Billy Ray Cyrus

Drawn By:
Matthieu Andre

TITLE:
Exploded View

SCALE: 1:10

02/19/2021

SHEET 2 OF 5

4

3

2

1

SOLIDWORKS Educational Product. For Instructional Use Only.

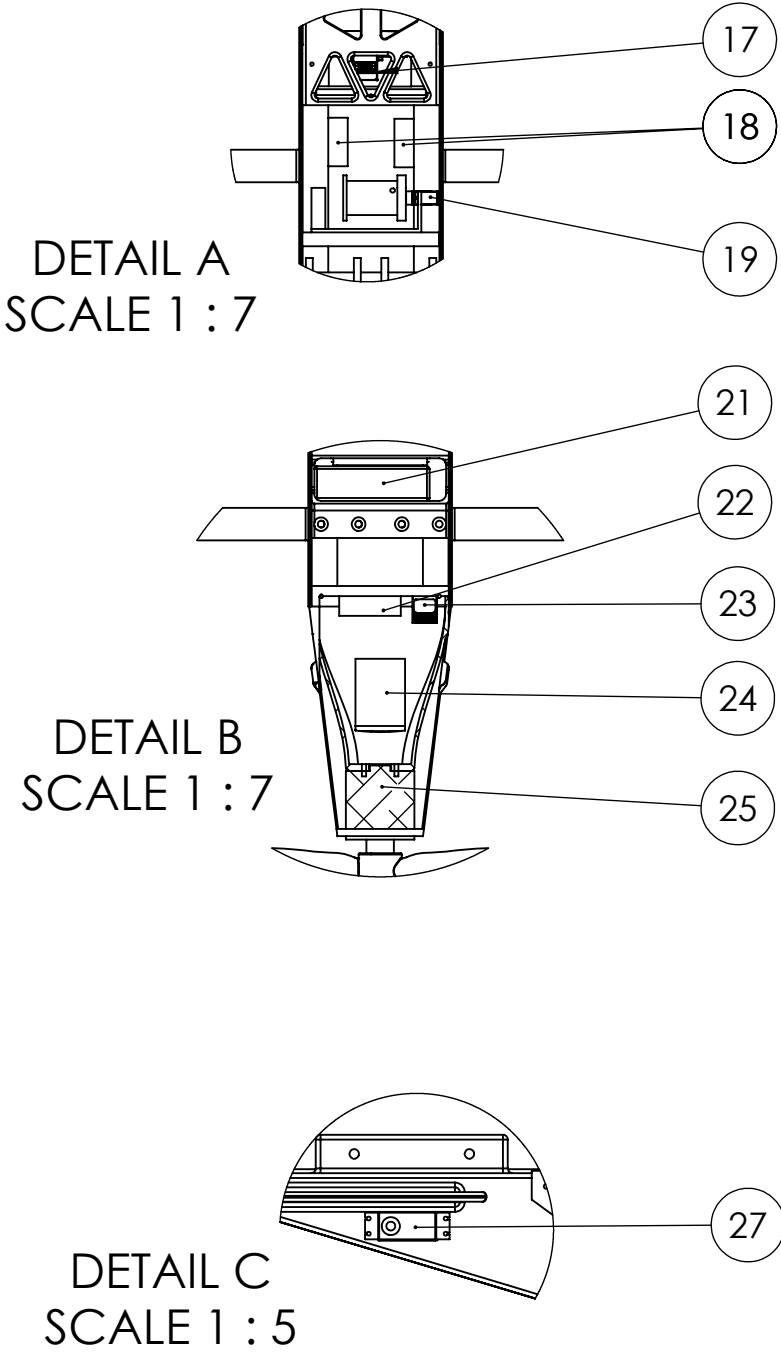
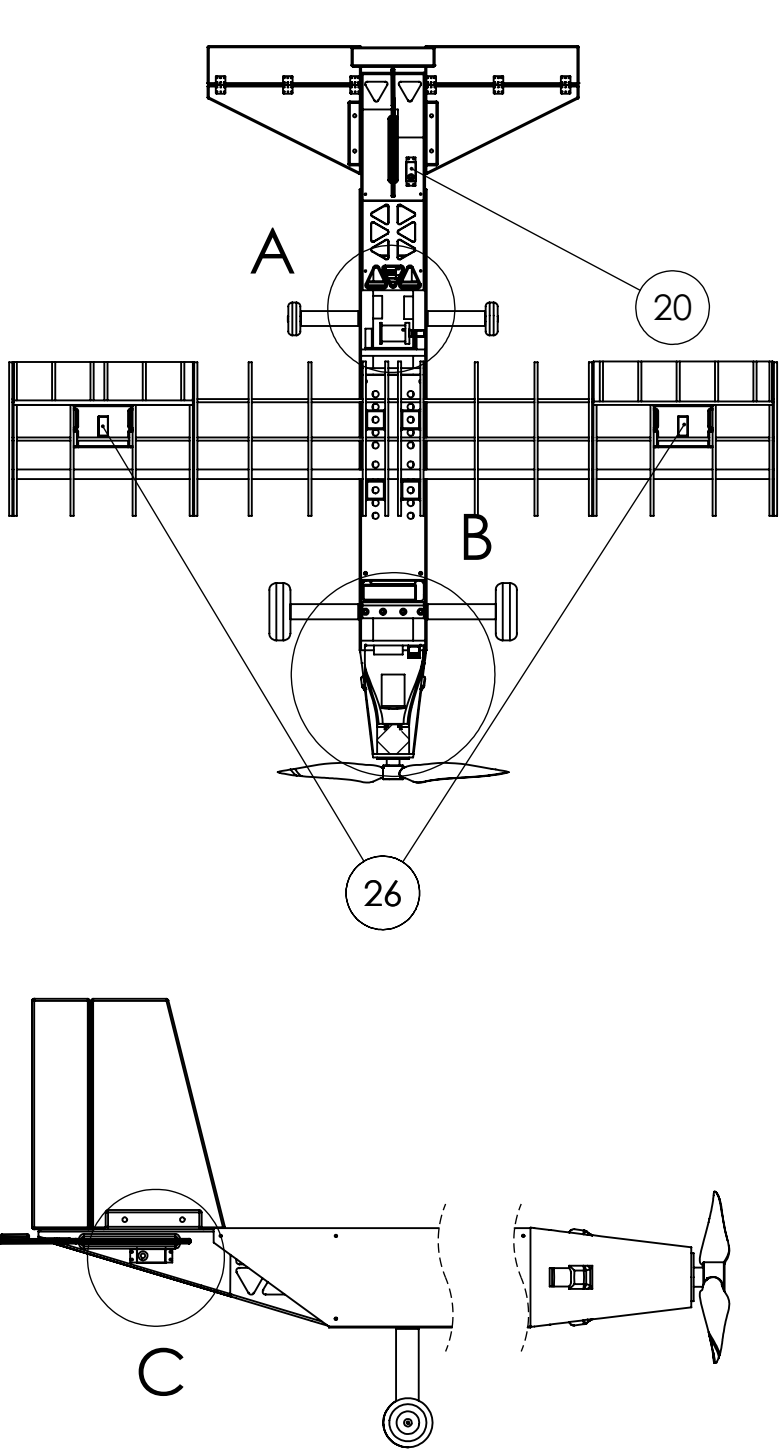
3

2

1

4				3				2				1			
Item No.	Part Name	Model	Qty.												
17	Door Servo	Tower Pro MG90S	1												
18	Arduino	Arduino Nano	2												
19	Winch Servo	Spektrum A6380	1												
20	Rudder Servo	Spektrum A6380	1												
21	Battery	Zippy Compact 4500mAh 10S 35C Lipo Pack w/ XT90	2												
22	BEC	YEP 20A HV SBEC	1												
23	Receiver	Spektrum AR8010T 8 ch receiver	1												
24	ESC	ZTW Gecko 120A ESC	1												
25	Motor	E-Flite Power 160	1												
26	Aileron Servo	Spektrum A6380	2												
27	Elevator Servo	Spektrum A6380	2												

Note: Elevator Servo mirrored on both sides of aircraft (Detail C)



George Washington University

Billy Ray Cyrus

Drawn By:
Matthieu Andre

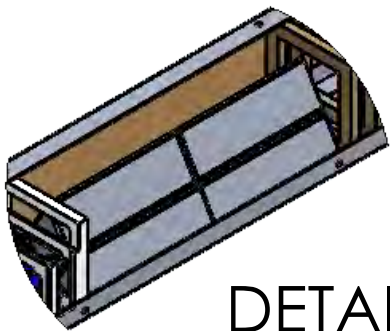
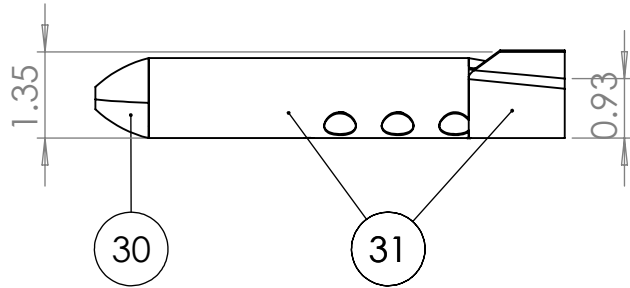
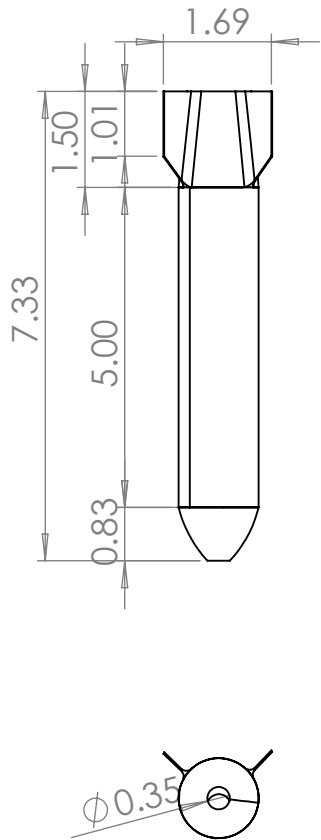
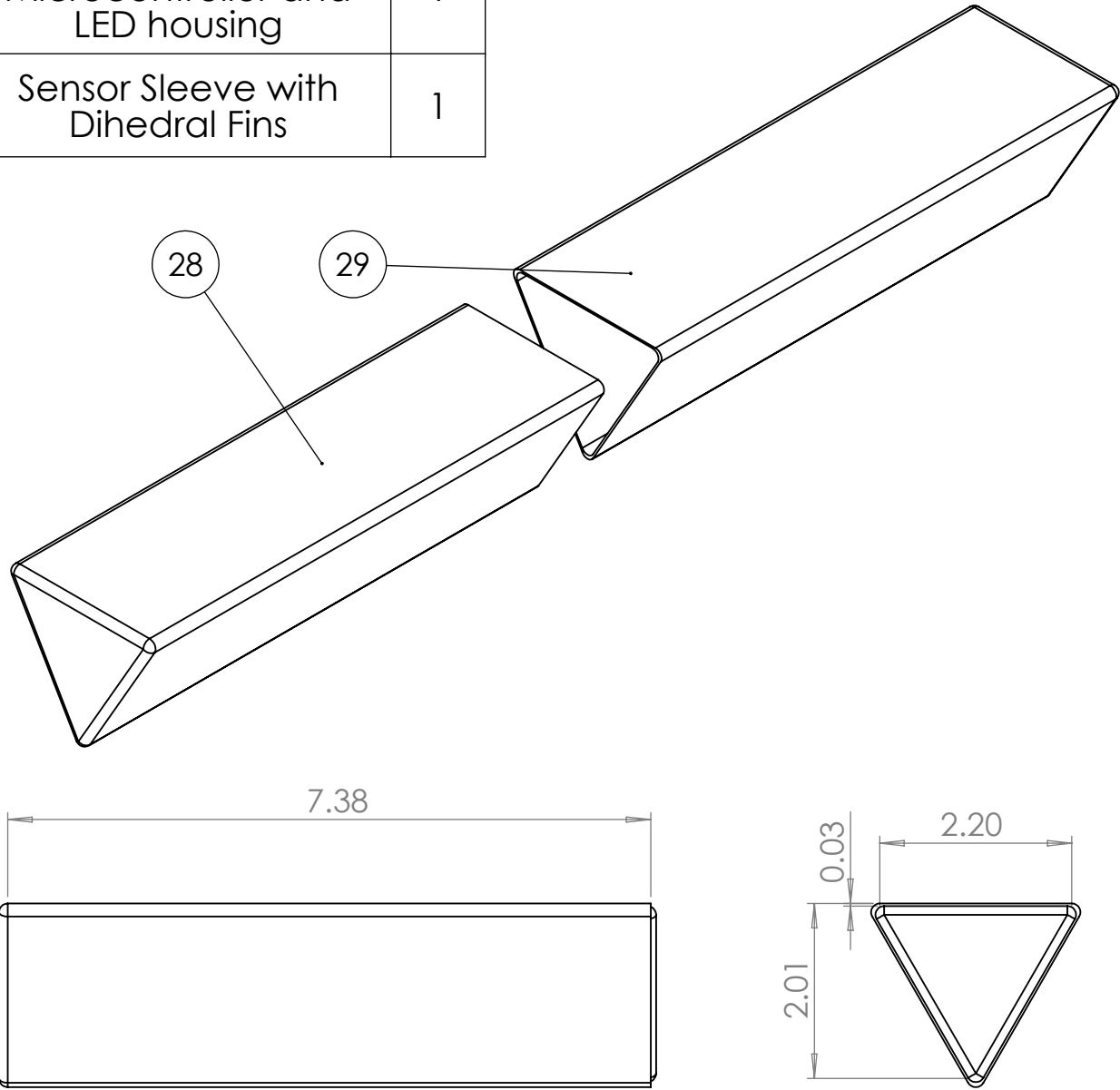
TITLE:
Control System Layout

SCALE: 1:15

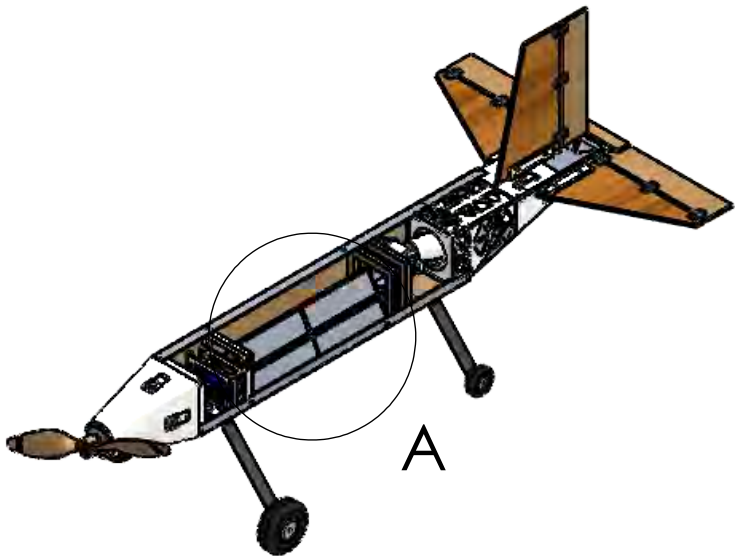
02/19/2021

SHEET 3 OF 5

Item No.	Part Name	Qty.
28	Shipping Container	1
29	Shipping Container Sleeve	1
30	Sensor Nose Cone with Microcontroller and LED housing	1
31	Sensor Sleeve with Dihedral Fins	1



DETAIL A
SCALE 1 : 8



Note: Units are in inches

George Washington University

Billy Ray Cyrus

Drawn By:
Jonathan Lee

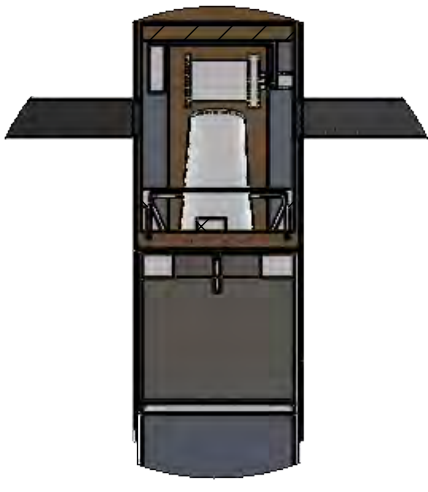
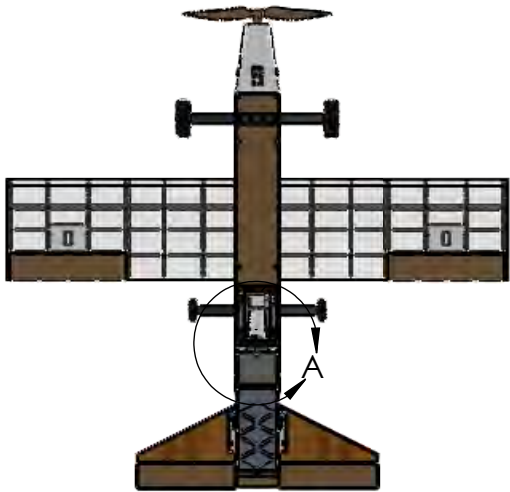
TITLE:
Sensor and Container

SCALE: 1:3

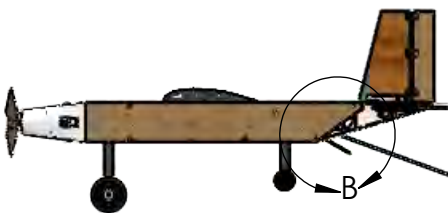
02/19/2021

SHEET 4 OF 5

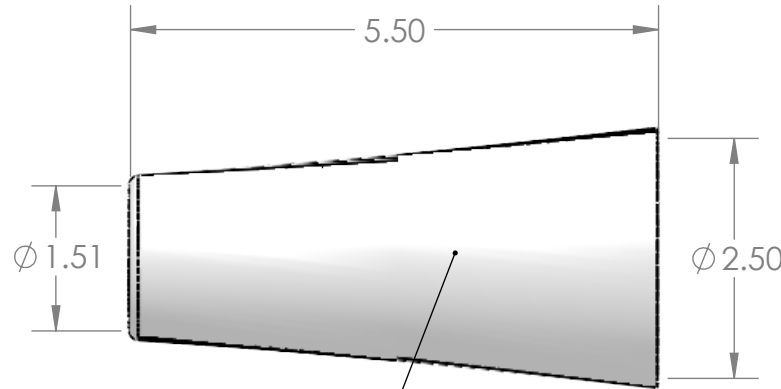
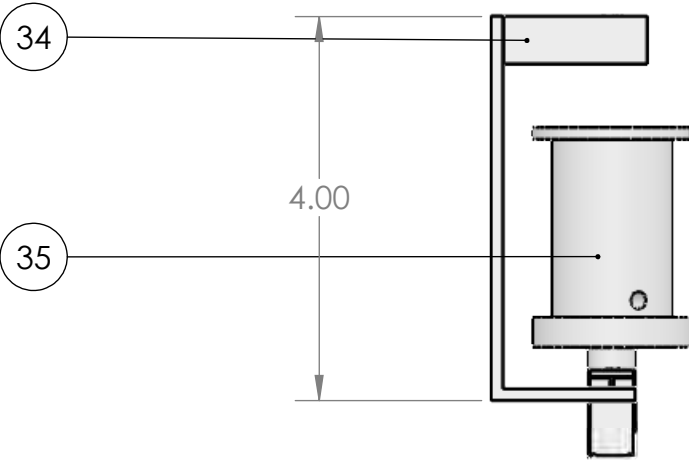
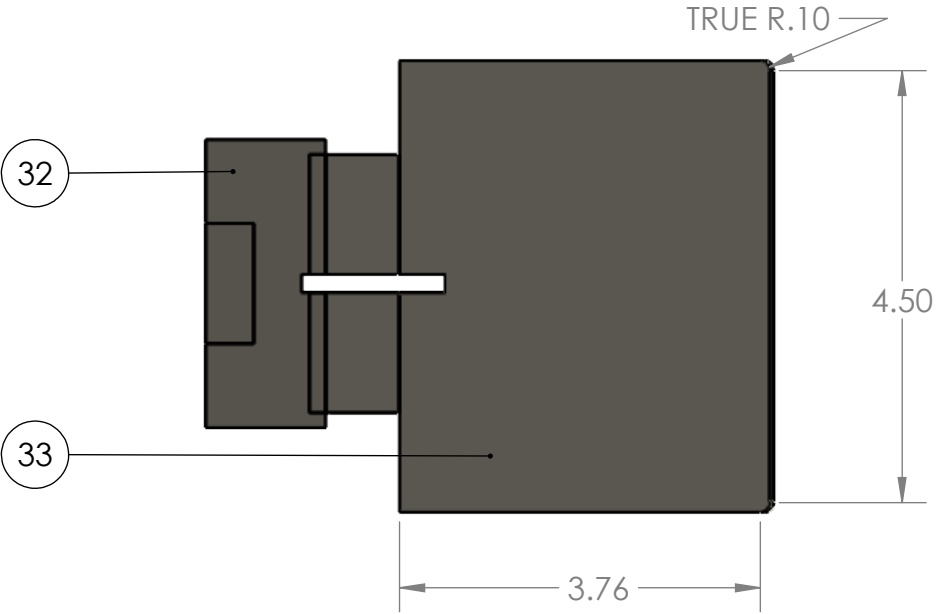
Item No.	Part Name	Qty.
32	Stile	1
33	Slab	1
34	Winch	1
35	Cable Drum	1
36	Audio Towing Cable	1
37	Sensor Docking Station	1



DETAIL A
SCALE 1 : 6



DETAIL B
SCALE 1 : 8



George Washington University

Billy Ray Cyrus

Drawn By:
Nii Adotey Sackar

TITLE:
Deployment System

SCALE: 1:2

02/19/2021

SHEET 5 OF 5

Note: Units are in inches

6. Manufacturing Plan

The team investigated multiple materials and manufacturing processes to construct the aircraft. The investigation evaluated the materials and processes based upon the sub system requirements detailed previously in the report and external limiting factors such as a condensed build time. This section outlines the results of the investigation and details the fabrication process for major aircraft components such as the wing, nose, empennage, fuselage, sensor, and sensor deployment and retrieval mechanism components.

6.1 Materials and Manufacturing Processes Investigated

6.1.1 3D Printing

3D printing provides the ability to produce complex components with easily customizable features including different material types and fill densities. The team has access to multiple Stratasys F170 HD printers and an Ultimaker S5s through the University. This could allow multiple components to be manufactured at once or for multiple copies to be batch-produced. The 3D printing services on campus are also free, making the process financially advantageous.

6.1.2 Balsa Wood

Balsa wood is commonly used to build RC aircraft because of its low density and high strength-to-weight ratio. Balsa also has good machinability as it can be laser cut, wire cut, sawed or cut with razor blades. Additionally, it is available in a variety of dimensions which makes it a favorable selection for many applications.

6.1.3 Plywood

Plywood is stronger than balsa wood and adds stability and support to aerostructures. Although plywood is heavier than balsa wood, thinner components can be used while maintaining necessary strength. Plywood also has good machinability with the ability to be laser cut or cut with multiple saw types (e.g. handsaw, bandsaw, tablesaw).

6.1.4 Carbon Fiber

Carbon fiber is the dominant composite material, known for its high strength to weight ratio. The machining of the raw material, however, is much more difficult than wood or soft metals. Carbon fiber is very expensive due to its intensive production process.

6.1.5 Aluminum

Aluminum offers higher strength and structural stability relative to commonly used RC aircraft materials. However, aluminum is much heavier. The machinability of aluminum is high because it can be cut by saws, machined with a drill press, turned on a lathe and easily finished with file, sandpaper, or grinding wheel.

6.1.6 Monokote

Many model aircraft use shrink-wrap on multiple components to improve aerodynamic surfaces. This shrink-wrapping material, Monokote, is extremely lightweight and inexpensive. The application process is well known and can be done on complex shapes, making it very advantageous to use on model aircraft components.

6.1.7 Adhesives & Connections

In addition to the main materials, the team considered the following adhesives and connectors for system integration: epoxy, super glue, cable ties, screws, threaded rods, nuts, and bolts. Epoxy is commonly used in RC models because of its easy application and impressive strength. However, they can only be used on components that do not need to be modular. Cable ties can be set easily, chained together, are easily removable and replaceable, and have a high strength. Screws, bolts and nuts provide high strength and are also easily interchangeable. However, these components can cause stress concentrations which can lead to cracked or splintered parts when the aircraft encounters significant loading. Screws, bolts, nuts, and cable ties can be used in similar applications. However, due to the increased weight and stress concentration of screws, bolts, and nuts, cable ties are preferred. Screws, bolts, and nuts were only used when increased strength was necessary, such as the landing gear integration into the fuselage.

6.1.8 Selection Process

The team decided on four criteria to evaluate material use: manufacturability, strength, weight, and cost. The criteria were determined based on the requirements and other relevant considerations. Table 6.1 shows the compared criteria for each considered material. Much of the aircraft design is modular, and each sub system has unique needs. As such, the material for each sub system will be determined based on the sub system's complexity, specific design requirements, and weight needs.

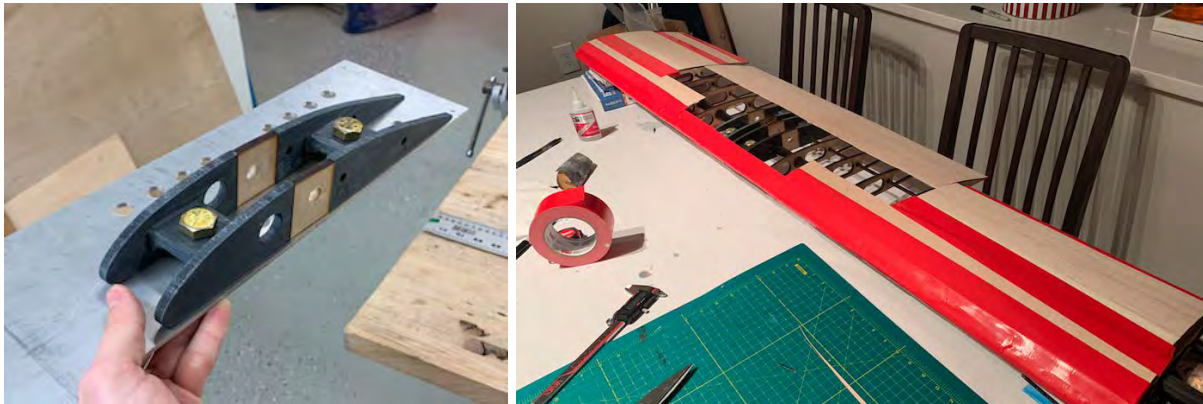
Table 6.1: Criteria Comparison for Material Selection

Criteria	Balsa Wood	Plywood	ABS	Carbon Fiber	Aluminum
Manufacturability	4	4	5	1	3
Strength	1	2	3	4	4
Weight	5	4	3	2	1
Cost	3	3	5	1	2

6.2 Major Component Manufacturing

6.2.1 Wing

The wing ribs and aileron tips were laser cut from plywood sheets. The mounting ribs and servo plates were 3D printed out of ABS due to their complexity. The two mounting rib pieces were glued to a laser cut plywood piece to make one full mounting rib. Carbon fiber spars were cut to length with a hand saw. Once the components were machined, the ribs were epoxied into their positions along the carbon fiber wing spars. Thin balsa wood sheets were used with duct tape to strengthen the leading edge of the airfoil and prevent dimpling in the Monokote. A thin balsa wood skin was also used to make the aileron control surface, and was glued to the plywood aileron tips. Wiring was run through the interior ribs to each servo plate. Then, shrink-wrap was applied over the wing to complete the airfoil shape, and holes were made under the mounting ribs to allow for electronic connections and fuselage mounting.



Figures 6.1A and 6.1B: Mounting Rib. Plate, and Wing Final Product

6.2.2 Fuselage

The plastic former and battery holder was 3D printed. Aluminum extruded angles were cut to length with a bandsaw and connection holes were drilled. Balsa wood formers were cut to shape with a saw. The formers were epoxied to the aluminum stringers on all four corners. After the interior of the fuselage was assembled and the fuselage was connected to the other sub systems. The fuselage was then wrapped in a skin. Originally the fuselage skin was constructed of balsa wood. However, the balsa wood began to crack during application so duct tape was utilized instead. The duct tape skin was flexible, allowing for easy application and accessibility to the interior of the fuselage. Nuts and bolts were used to connect the front and rear landing gear directly to the aluminum stringers.



Figures 6.2A and 6.2B: Fuselage Inner Assembly and Landing Gear Attachment

6.2.3 Nose

Due to the complexity of the nose cone, 3D printing was utilized. ABS was selected as it was readily available and strong enough to counteract the torque from the propeller. The motor was mounted to the nose cone structure with the factory screws and connected to the ESC and BEC, both of which were duct taped inside the cone. Finally, the nose was connected to the fuselage stringers with screws and bolts.



Figure 6.3: Nose Cone with Motor Installed

6.2.4 Empennage

To address the complexity of the empennage shape, the main tailcone section was 3D printed. ABS plastic was utilized, as it was readily available and had good structural characteristics. The tail cone body was made in two separate parts due to limitations in printing size. The two 3D printed pieces were attached with screws at their connection points. The stabilizers were made of laser cut plywood and secured on the empennage with screws and bolts. The rudder and elevators were made of appropriately sized balsa wood and connected to the stabilizers with RC aircraft hinges. Additionally, a balsa connection piece was attached to span the space between elevator sections.



Figure 6.4: Full Empennage (resting on its side)

6.2.5 Sensor and Container

The sensor electronics tray and outer sleeve were made from 3D printed ABS plastic. 3D printing was used due to the complexity of the sensor shape, tight tolerances, and low cost. After printing the walled tubes and interlocking components, the components were sanded and assembled using super glue. The sensor electronics were soldered

together using silicon wire for its flexibility. The shipping containers were also 3D printed using ABS to take the impact of the loading. The container prints are shown in Figure 6.5. Foam was installed into the shipping containers to protect the sensors from drop shock events. During tests, duct tape secured the lid of the container.



Figure 6.5: Assembled Sensor and 3D Print of Sensor Container

6.2.6 Sensor deployment mechanism

The cargo door was made of foam board to save weight while preserving necessary structural integrity. The foam board was laser cut to the required shape and the living hinge system was installed. The opening pistons were made from 3D printed PLA plastic. The sensor docking station was 3D printed with ABS plastic. Balsa wood sheets were epoxied to the large hole of the cylinder to help it sit in the empennage. The cable drum and winch mount were also 3D printed with ABS. A carbon fiber rod was inserted into the cutout holes of the mount and the cable drum to join the two parts. The winch mount was epoxied to the wooden formers in the fuselage.

6.3 Manufacturing Gantt Chart

A manufacturing Gantt chart was created to ensure the team met the required two week construction timeline set in the requirements. However, limitations placed on the team due to COVID, required some processes to begin before the two week build. These processes are shown in the asynchronous week section of the chart.

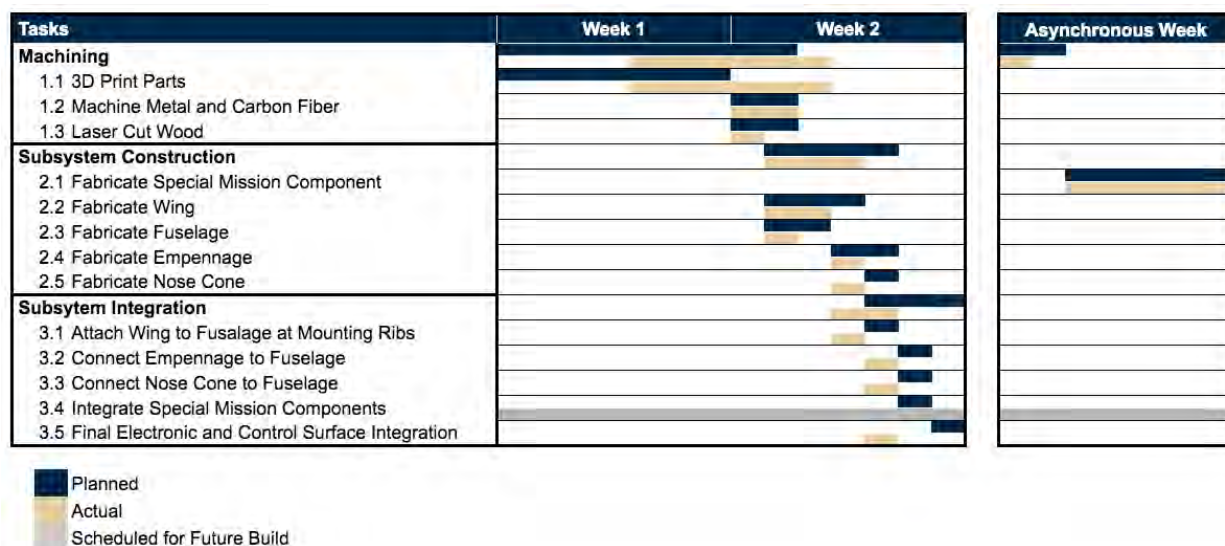


Figure 6.6: Manufacturing Plan Gantt Chart

7. Testing Plan

The testing program consisted of three phases. Phase 1 was simulation and model testing, Phase 2 was tabletop modeling and creating working prototypes of sub system components, and Phase 3 was flight testing. Phase 1 testing was primarily discussed in the design sections of the report, as the tests were performed and relevant data was collected during the design phases. This section outlines all the ground tests and test flights that were performed and planned to be performed. It includes a testing schedule, objectives for each test, data collected, data application, and test and flight checklists. Due to challenges faced with COVID and GW classes being held fully online, the team was not able to complete ground or flight tests for the special mission components or propulsion system.

7.1. Ground Testing

7.1.1 Sensor Aerodynamic Characteristics Testing

Sensor flight tests were conducted during the months of December and January to determine the aerodynamic stability of the various sensor designs at different air speeds for the sensor fin shape selection process (see Section 3.4.6). Data collected from the tests was analyzed to finalize sensor fin shape and determine flight characteristics, including average tow cable angle and standard deviation (ie. correlated with stability). The testing procedure is detailed below.

The sensor was mounted to a bike on the roof of a car as seen in Figure 7.1A. The tow cable was attached to the bike handlebar to reduce the impact of buffeting airflow coming over the car. For each test, the car would accelerate to and hold the testing speed for the duration of the test. The test route was a straight stretch of road, seen in Figure 7.1B. Each sensor design was tested in intervals from 30-60 mph. Data was collected from a roof mounted video camera and a 9-axis IMU embedded in the sensor. Another sensor mounted to the car collected baseline data including GPS coordinates and heading.



Figures 7.1A and 7.1B: Testing Rig and Map of Test Route with GPS Overlay

7.1.2 Propulsion Testing

Tests to measure the maximum thrust, power draw, and amp draw from the motor at various stages of flight will be conducted in March. The motor will be mounted and attached to a spring scale, and a watt meter will be connected in series with the power system. The mock pilot will run the motor for a mock flight, simulating the power inputs that are expected during flight. A second test team member will measure the maximum thrust, power drawn, and amps drawn at the following phases of the mock flight: takeoff, climb, cruise, descent, and landing.

7.1.3 Sensor Shipping Container Drop Testing

A drop test will be conducted in March to ensure that the shipping container can protect the sensor from drop shock events. The sensor will be packed in the shipping container and dropped from a height of 10 in onto each face and a rounded corner connecting two the rectangular faces. Then, the sensor will be powered up and tested to verify operability.

7.1.4 Sensor Deployment and Retrieval System Testing

Range of motion tests will be conducted on the cargo door in March. The capabilities of the pistons and the servos used to open and close the door, the durability of the living hinge, and clearance for the sensor deployment and retrieval will be tested. The door's continuous rotation servo will be given a command to drive the door open until the door slab is 0°, 20°, and 30° below horizontal. Two tests will be conducted on the winch: the first without weight and the second with the sensor attached to the audio cable. The winch will unspool the tow cable to full length and then retrieve the cable, spooling onto the drum. The number of rotations necessary and torque requirements both with and without weight will be observed. Additionally, the cable and servo strengths will be tested using the applied weight experiment.

7.2 Flight Testing

Phase 3 of the testing program encompassed all performance and mission relevant field and flight tests. This ranged from a full series of ground tests to full scale pattern execution in highly loaded configurations. A build up approach was used in each test event to minimize risk associated with damage to the aircraft and safety of the test crew. A test matrix and test cards were utilized to plan tests, communicate procedure, and record data. Table 7.1 shows an example of a test matrix layout and Figure 7.1 shows a sample test card. This was completed for each round of testing outlined in the following sections.

Table 7.1: Flight Test 1 Matrix

Event	Test	Speed (Target)	Altitude (Target)	Basic Procedure	Validation/ Evaluation Criteria
1	Controls Validation	0 ft/s	Surface	Input commands to control surfaces without the motor on and observe the behavior of the controls surfaces	Control surfaces behavior correctly corresponds to each input
2	Slow Speed Taxi	0 - 15 ft/s	Surface	Taxi at low end of ground speed range and input commands to controls surfaces	The aircraft responds to commands with the appropriate magnitude and in a timely manner
3	Mid Speed Taxi	15 - 30 ft/s	Surface	Taxi at middle of ground speed range and input commands to control surfaces	The aircraft responds to commands with the appropriate magnitude and in a timely manner

Test: High Speed Taxi	Target Speed: 30- 50 ft/s Target Altitude: Surface
Procedure	Comments
<ol style="list-style-type: none"> 1. Slowly open to $\frac{3}{4}$ throttle to accelerate down the runway until operating at around 40 ft/s 2. Carefully input right turn commands (aileron and rudder) 3. Back off controls input, recenter with left turn commands 4. Once straight, carefully input left turns commands (aileron and rudder) 5. Back off controls input, recenter with right turn commands 6. Close throttle 	<p>Conditions: No more than a 5 mph wind, temperatures no lower than 15°F</p> <p>Notes:</p> <ul style="list-style-type: none"> • Left turning tendency prominent at high speeds • Rudder input is effective • Slight delay on turning after rudder command is given • Satisfactory steering control during taxi

Figure 7.2: Test Card Sample

7.2.1 Taxi Testing and Checklist

Flight Test 1 included a full range of taxi tests to verify rudder control on a four wheel landing gear configuration. Hop tests, where the aircraft was flown roughly 100 ft from takeoff at 6 ft off the ground then landed, were also performed to verify takeoff and landing capabilities before a full flight event. The checklist was a critical component in determining go-no go for every event. If any item was not verifiable, the event would be postponed.

7.2.2 Empty Weight Flight Testing

Flight Test 1.5 consisted of two events, a trim flight and a pattern flight. Both events were empty aircraft, meaning there was no additional cargo like what would be present in Mission 2. The trim flight was used to determine the trim configuration at which the aircraft could maintain straight and level flight after takeoff. The second event was a simple looped pattern execution with additional pitching and rolling maneuvers to verify aileron and elevator capabilities. The pre-flight checklist for this test is shown in Table 7.2.

Table 7.2: Pre-Flight Checklist

Component	Check
Nose Cone	<input type="checkbox"/> Battery is charged, secured, and connected to motor <input type="checkbox"/> Receiver is wired properly to connections
Fuselage	<input type="checkbox"/> CG is appropriately placed and aircraft is balanced <input type="checkbox"/> All internal components are secured
Landing Gear	<input type="checkbox"/> Wheels are correctly oriented
Control Surfaces	<input type="checkbox"/> All transmitter inputs produce the correct control surface movement

7.2.3 Mission Testing

Tests for the Ground Mission and Mission 1 were performed in Flights Tests 1 and 1.5. Tests for Missions 2 and 3 are slated for later in the year when there are fewer weather constraints. The Mission 2 and 3 tests will follow the same general procedure as Mission 1 to keep data points consistent across configurations, but they will have slight alterations to validate mission requirements. For example, in Mission 3, there will be a full execution of a 10 minute flight whereas Mission 1 testing only had a 2 minute flight. Due to location, weather, and time constraints, performance testing will be built into the framework of each mission test. For example, while testing Mission 1 capabilities, additional rolling and pitching maneuvers were planned into the pattern to collect data on roll rate and pitch recovery. Flight tests 2 and 3 will have similar test methods for each configuration. New checklists for each mission will be developed prior to testing.

7.3 Schedule

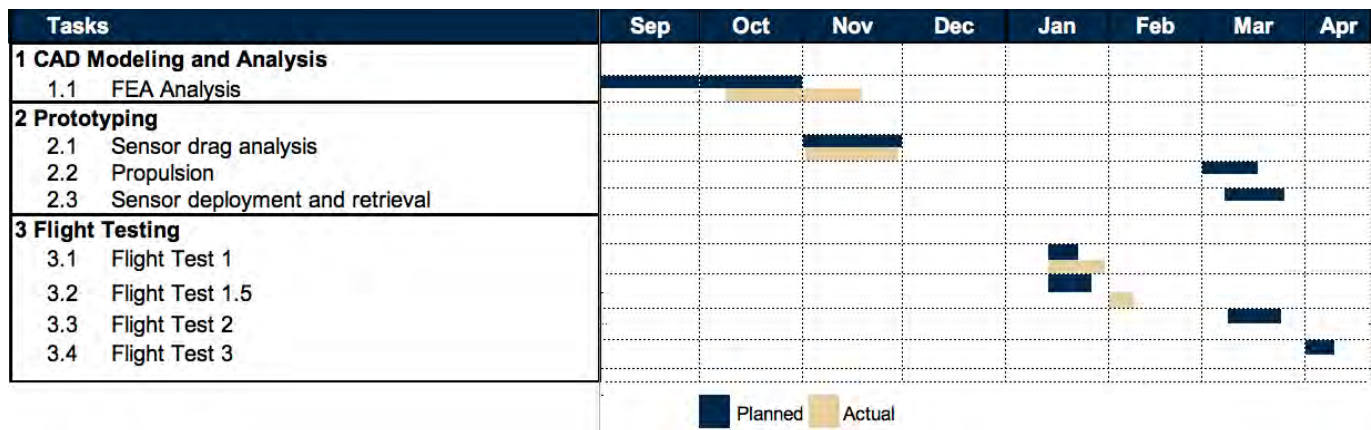


Figure 7.3: Testing Schedule

8. Performance Results

After completion of modeling and prototype testing, flight tests 1 and 1.5 allowed for airframe validation testing. Empty aircraft flight testing validated the design's capability for stable and reliable flight. Due to scheduling constraints, mission specific testing has not been completed yet, but each test will be geared towards optimizing the mission with the performance capabilities of the airframe.

8.1 Special Mission Component Testing Results

Sensor aerodynamic behavior was captured and is plotted onto a position scatter plot, showing the positions of the sensor relative to the car's inertial reference frame. Figures X-Z below show the average angle of inclination and standard deviation of each sensor design. The lower the standard deviation of the tow cable angle, the more stable the sensor was. The dihedral design had the best performance of the bunch, with the lowest variance in tow cable angle. It also maintained the lowest angle from the vertical. The other sensors struggled to maintain a consistent heading, and were therefore not stable designs. This information gave the team critical quantitative measurements to aid in selecting the dihedral design (see 3.4.6).

Additionally, the testing results can be used to verify initial drag estimates. The experimental data is analyzed to determine the sensor's actual coefficient of drag. Comparing the actual coefficient of drag to the estimated coefficient of drag from Section 4.2.8 can provide information on the quality of the estimations made. The analysis was conducted on the test with the most calibrated data points at 70 ft/s and 34° from horizontal. The team measured $C_{d, \text{ actual}} = 0.293$. The sensor's actual coefficient of drag has a 9.29% error from the estimated $C_{d, \text{ est}} = 0.323$. This percent error is deemed acceptable given the variability of doing a real world test.

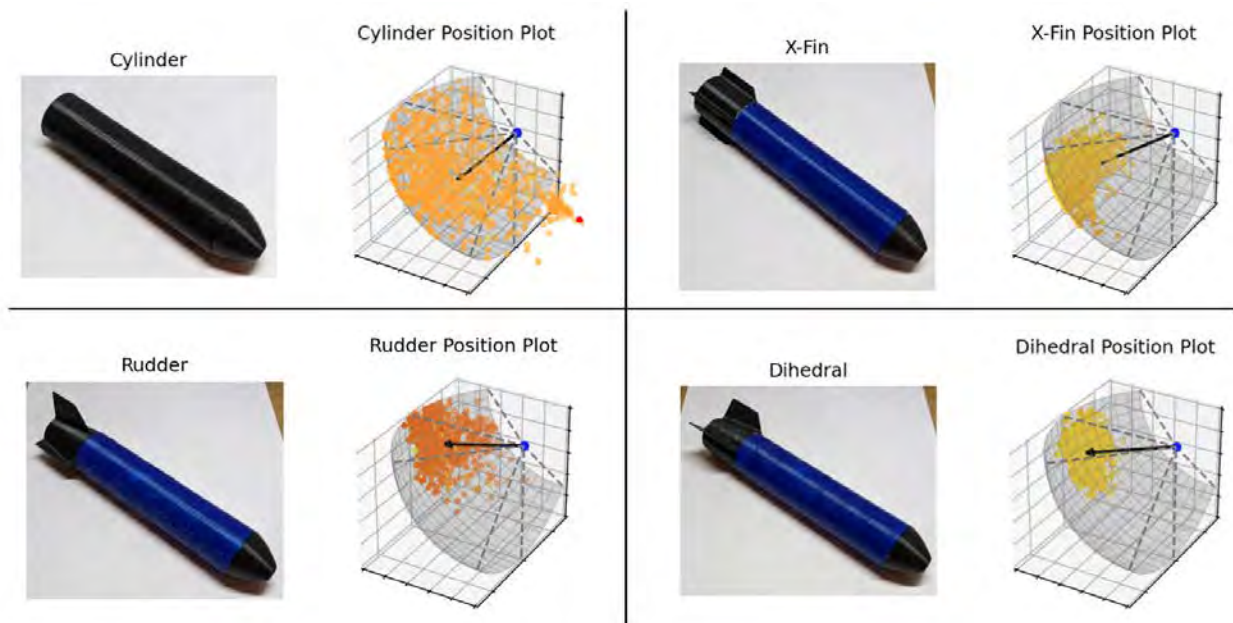


Figure 8.1: Sensor Fin Designs with Position Plots

8.2 Flight Testing Results

All flight test analyses were conducted using observational data and pilot comments during flight. These three components were enough to validate our design configuration and obtain baseline performance data.

8.2.1 Taxi Testing Results

Taxi testing demonstrated that the landing gear's four-wheel configuration had minimal effect on rudder controlled steering. While there was a slight input delay it was not significant enough to warrant a redesign of the landing gear. The landing gear proved to be an important stability factor. Hop testing revealed that on takeoff the aircraft had a left rolling tendency and struggled to maintain straight and level flight. On each takeoff the aircraft was consistently tail heavy.



Figure 8.2: Billy Ray During a Fast Taxi Test

8.2.2 Empty Weight Flight Testing Results and Data

After the taxi tests, a lighter weight empennage structure was installed to reduce tailweight. The empty aircraft flew two empty weight flights: one trim flight and one performance testing flight. The aircraft demonstrated straight and level flight is possible given the loading and configuration. The airframe is slightly pitch sensitive, but this was fixed easily with trimming. The pattern flight showed stability not only in straight and level flight but also in banked turns. Most turns were around 30° angle of bank, but even at 45° the aircraft showed no signs of sideslip or adverse yaw. In a crosswind, a yawing moment was present specifically in the empennage, but it was easily correctable with rudder input.

Table 8.1: Aircraft Empty Weight Flight Test Results

	Estimate	Actual	Error
Weight (lbf)	13	17	30.77%
Cruise Velocity (ft/s)	51.96	73.3	41.07%
Lap Time (s)	68.7	54	-21.40%

The cruise velocity and lap time was measured through video analysis and are shown in Table 8.1. The aircraft had a significantly higher cruise velocity than expected, which reduced the empty weight flight test time by a little over 20%. This is likely due to the aircraft being around four pounds heavier than anticipated due to challenges during integration. While being overweight is not ideal, this does verify the design should have little issue carrying 3 lb of cargo, as it flew well for

being 4 lbs overweight. Slight design modifications will be made to future builds to ensure the aircraft weight is closer to the target weight. Additionally, the team will consider delivering more sensor shipping containers than previously planned. Pictures of the aircraft during the flight test are shown in Figures 8.3 and 8.4.



Figure 8.3: Billy Ray On the Ground



Figure 8.4: Billy Ray Climbing After Takeoff

9. Bibliography

- [1] Raymer, D. P., *Aircraft Design: A Conceptual Approach*, 5th ed., AIAA, Virginia, 2012.
- [2] Hoseini, S. H., "Swept Wing Configuration", Sharif University Department of Aerospace Engineering.
- [3] Obert, E., *Aerodynamic Design of Transport Aircraft*, Delft University of Technology, 2009.
- [4] Sadraey, M. H., *Aircraft Design: A Systems Engineering Approach*, Wiley, Nov 2012.
- [5] "Airfoil database", Airfoil tools [online database], <http://airfoiltools.com/> [retrieved 26 September 2020].
- [6] Sadraey, M. H., *Aircraft Performance: An Engineering Approach*, 1st ed., CRC Press, 2017.
- [7] "The *Watts Per Pound* rule", RC Airplane World [online webpage], <http://rc-airplane-world.com/>.
- [8] "Static Thrust Calculator", Godollo Airport [online webpage], http://godolloairport.hu/calc/strc_eng/index.htm.
- [9] "Estimate Propeller's Static Thrust", RC Planes [online webpage], https://rcplanes.online/calc_thrust.htm.
- [10] "AVL", Massachusetts Institute of Technology, 2017, <https://web.mit.edu/drela/Public/web/avl/>.
- [11] How, J. P., "Aircraft Stability and Control", Massachusetts Institute of Technology OpenCourseWare, 2004.
- [12] "Dynamic Stability", Cornell University, MAE 5070.